The energetics of flow through a rapidly oscillating tube. Part 2. Application to an elliptical tube

ROBERT J. WHITTAKER[1], MATTHIAS HEIL[2], JONATHAN BOYLE[2], OLIVER E. JENSEN[3] AND SARAH L. WATERS[1]

[1]Oxford Centre for Industrial and Applied Mathematics, University of Oxford, 24–29 St Giles', Oxford OX1 3LB, UK

[2]School of Mathematics, University of Manchester, Oxford Road, Manchester M13 9PL, UK

[3]School of Mathematical Sciences, University of Nottingham, University Park, Nottingham NG7 2RD, UK

In Part 1 of this work, we derived general asymptotic results for the three-dimensional flow field and energy fluxes for flow within a tube whose walls perform prescribed small-amplitude periodic oscillations of high frequency and large axial wavelength. In the current paper, we illustrate how these results can be applied to the case of flow through a finite-length axially non-uniform tube of elliptical cross-section – a model of flow in a Starling resistor. The results of numerical simulations for three model problems (an axially uniform tube under pressure–flux and pressure–pressure boundary conditions and an axially non-uniform tube with prescribed flux) with prescribed wall motion are compared with the theoretical predictions made in Part 1, each showing excellent agreement. When upstream and downstream pressures are prescribed, we show how the mean flux adjusts slowly under the action of Reynolds stresses using a multiple-scale analysis. We test the asymptotic expressions obtained for the mean energy transfer E from the flow to the wall over a period of the motion. In particular, the critical point at which $E = 0$ is predicted accurately: this point corresponds to energetically neutral oscillations, the condition which is relevant to the onset of global instability in the Starling resistor.

1. Introduction

Flows through flexible tubes and channels have widespread biological applications, notably in the respiratory and cardiovascular systems (Grotberg & Jensen 2004). They are of particular fluid-mechanical interest because of the diverse instabilities that can arise in such systems. In addition to intrinsic hydrodynamic instabilities that can be manipulated using compliant walls (Davies & Carpenter 1997), a variety of instabilities originate through direct interaction between the flow and the deformable wall. The canonical experimental device for investigating such instabilities is the Starling resistor, in which a flow is driven through a finite length of externally pressurized flexible tube that is mounted between rigid supports (e.g. Bertram 2003; Bertram & Tscherry 2006). The present paper contributes to attempts by

researchers over many years to develop a full understanding of the mechanisms by which the three-dimensional flow in a Starling resistor loses stability to self-excited oscillations.

Previous theoretical models have largely considered simplified models of this system in zero-, one- and two-dimensional formulations. Although low-dimensional models are inevitably inaccurate in many respects, a broadly consistent picture emerges from these studies. In the absence of wall inertia and assuming the internal flow is laminar but at moderately high Reynolds number, the system can lose stability to multiple modes of oscillation. One-dimensional models show how a supported flexible tube in a non-uniform configuration (typically being collapsed towards its downstream end) loses stability to modes with two, three or more extrema in the axial distribution of wall displacement (Jensen 1990), with each mode falling into a distinct frequency band. Modes with similar characteristics have recently been reported in simulations of a two-dimensional channel analogue of the Starling resistor (Luo *et al.* 2008), although these are accompanied by the excitation of internal Tollmien–Schlichting waves. High-frequency mode-1 instabilities (with a single extremum in displacement amplitude) have also been predicted by both one- and two-dimensional models of the Starling resistor system when the axial tension in the flexible segment is large (Jensen & Heil 2003; Stewart, Waters & Jensen 2009), although direct experimental evidence for this class of instability is not yet available.

The mechanism responsible for the mode-1 instability was revealed by detailed asymptotic analysis of the two-dimensional model system, supported by computational simulation (Jensen & Heil 2003). Typically the experimental system is asymmetric (either the upstream and downstream rigid supports differ in length, or different boundary conditions are applied at the two tube ends). Rapid inward and outward motion of the flexible wall can induce axial inviscid sloshing of the core flow, which is superimposed on the mean flow through the channel. If the sloshing is of larger amplitude at the upstream end of the system, it is possible for a net flux of kinetic energy to be extracted from the mean flow in order to sustain self-excited oscillations of the wall. Threshold asymptotic criteria for the onset of self-excited mode-1 oscillations were identified in both one- and two-dimensional models, involving a balance between kinetic energy flux and viscous dissipation in Stokes layers (Jensen & Heil 2003; Stewart *et al.* 2009).

It is natural to ask whether the mode-1 instability mechanism identified in one- and two-dimensional models applies also in three dimensions. Rather than considering full flow–structure interaction, this question can be addressed by imposing prescribed wall displacements to a finite-length tube under axial boundary conditions relevant to the Starling resistor (i.e. either pressure or flux conditions) and assessing the overall energy budget of the system. A necessary, but not sufficient, condition for instability through the mode-1 mechanism is for there to be a net time-averaged flux of energy from the flow to the wall. Choosing wall displacements that mimic modes of a flexible shell then provides a useful indication of the likelihood of genuine instability. Heil & Waters (2006) took this approach by examining small-amplitude non-axisymmetric displacements to a circular tube. They focused attention on the cross-sectional flows driven by these displacements. Although such displacements resemble the primary buckling instability of an elastic tube, the cross-sectional area changes are quadratic in displacement amplitude, and therefore the induced sloshing flows are too weak to draw energy into the wall within the parameter regime studied. However, if the oscillations occur about a non-axisymmetrically buckled steady configuration, Heil

& Waters (2008) showed via direct simulation that the induced sloshing flows are sufficiently vigorous to extract energy from the mean flow (after averaging over oscillations). Their computations indicated that for this to be the case, α/St should exceed a threshold value dependent on the particular profile of the oscillations. Here $St = a/\mathscr{U}T$ is the Strouhal number of the mean flow $\mathscr{U}$ through a tube of initial mean radius a and $\alpha = a(\rho/\mu T)^{1/2}$ is the Womersley number associated with wall oscillations of period T; ρ and μ are the fluid density and viscosity. Heil & Waters (2008) provided a scaling argument that explained the observed behaviour.

In Part 1 of the current study (Whittaker *et al.* 2010), we used asymptotic methods to identify a general, and remarkably simple, criterion for prescribed small-amplitude high-frequency long-wavelength oscillations to extract zero time-averaged energy from the mean flow. This criterion is (9.5) in Part 1, which is reproduced below as (2.13*b*) and (2.17*b*) for two special cases. In addition to St, α and $\ell = L/a$, where L is the tube length, the expression involves only simple geometric quantities that can be computed once the form of the oscillation has been prescribed. The zero-energy-transfer threshold applies in the distinguished limit $1 \ll \alpha \sim \ell St \sim \ell^2$, for arbitrarily small oscillation amplitude. While this work was motivated by a possible axial-mode-1 instability mechanism, the results of Part 1 are valid for arbitrary (long-wavelength) deformation profiles and indicate that it is possible for higher-order axial modes to exhibit instability too.

The aim of the present paper is to test this formula against numerical simulations of the three-dimensional flow through an oscillating tube, with both pressure and volume-flux boundary conditions at the tube ends. The walls of the tube are subjected to periodic oscillations with an azimuthal wavenumber of 2 and axially varying amplitude. The initial tube shape, about which the oscillations occur, is termed the 'steady configuration'. To ensure that vigorous axial sloshing is induced, a non-axisymmetric steady configuration is chosen. Specifically we shall consider tubes of elliptical cross-section (possibly axially varying) in the examples that follow.

In §2 we describe the general set-up for the flow through a collapsible tube and briefly review the key results obtained in Part 1. In §3 we define a particular tube shape and oscillation profile and describe the asymptotic and numerical techniques employed. Results and comparison for the cases of an axially uniform steady configuration with pressure–flux and pressure–pressure conditions are presented in §§4 and 5 respectively. Results and comparison for an axially varying steady configuration subject to pressure–flux boundary conditions are presented in §6. Finally, we make some concluding remarks in §7.

2. General set-up and key results from Part 1

We consider a tube of length L and typical diameter $2a$, containing a Newtonian fluid of density ρ and dynamic viscosity μ. Boundary conditions applied at the ends drive a mean axial flow, with cross-sectionally averaged velocity $\mathscr{U}$ at the upstream end. Sections of the tube adjacent to each end are assumed to be rigid and therefore do not deform. The central section undergoes prescribed small-amplitude periodic oscillations of typical amplitude $a\Delta$ and time scale T (see figure 1*a*).
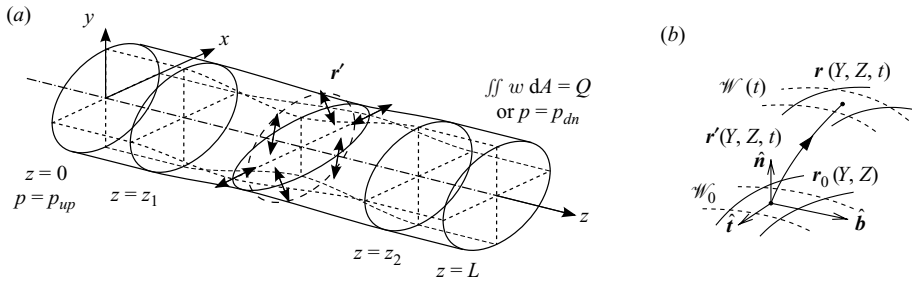
FIGURE 1. (*a*) A sketch of the elliptical tube configuration used in the numerical simulations described in the present paper. The rigid sections occupy $0 < z < z_1$ and $z_2 < z < L$, and the central section undergoes oscillations described by the displacement vector $\boldsymbol{r}'$. The mean flow is from left to right, driven either by an imposed pressure drop or a flux condition at the downstream end. (*b*) A close-up of the upper surface of the tube, depicting the triad of unit vectors $(\hat{\boldsymbol{n}}, \hat{\boldsymbol{t}}, \hat{\boldsymbol{b}})$ aligned with the surface $\mathscr{W}_0$ in the steady configuration, and the displacement vector $\boldsymbol{r}' = \boldsymbol{r} - \boldsymbol{r}_0$.

2.1. *Notation and parameter regime*

The fluid velocity $\boldsymbol{u}$ and pressure p within the tube are governed by the Navier–Stokes equations:

$$\nabla \cdot \boldsymbol{u} = 0, \tag{2.1a}$$

$$\rho \left(\frac{\partial \boldsymbol{u}}{\partial t} + (\boldsymbol{u} \cdot \nabla)\boldsymbol{u} \right) = -\nabla p + \mu \nabla^2 \boldsymbol{u}. \tag{2.1b}$$

The centreline of the tube is located on the z-axis, with the upstream and downstream ends located at $z = 0$ and $z = L$ respectively. We parameterize the tube wall by two Lagrangian coordinates (Y, Z), such that the position vector to a material point on the moving tube wall $\mathscr{W}(t)$ is given by

$$\boldsymbol{r}(Y, Z, t) = \boldsymbol{r}_0(Y, Z) + \boldsymbol{r}'(Y, Z, t), \tag{2.2}$$

where $\boldsymbol{r}_0(Y, Z)$ parameterizes the steady configuration $\mathscr{W}_0$, while the time-periodic wall deformation is described by the displacement vector $\boldsymbol{r}'$.

We define a right-handed orthonormal triad of unit vectors $(\hat{\boldsymbol{n}}, \hat{\boldsymbol{t}}, \hat{\boldsymbol{b}})$ aligned with the surface $\mathscr{W}_0$, so that $\hat{\boldsymbol{n}}$ is the outward-pointing normal, $\hat{\boldsymbol{t}} \cdot \hat{\boldsymbol{z}} = 0$ and $\hat{\boldsymbol{b}} \cdot \hat{\boldsymbol{z}} > 0$ (see figure 1*b*). The displacement vector $\boldsymbol{r}'$ is then decomposed as

$$\boldsymbol{r}'(Y, Z, t) = a\Delta \, \mathrm{Re}\left[\left(\xi(Y, Z)\, \hat{\boldsymbol{n}} + \eta(Y, Z)\, \hat{\boldsymbol{t}} + \frac{a}{L}\zeta(Y, Z)\, \hat{\boldsymbol{b}} \right) \mathrm{e}^{\mathrm{i}\omega t} \right], \tag{2.3}$$

for some complex-valued functions $\xi(Y, Z)$, $\eta(Y, Z)$ and $\zeta(Y, Z)$ where Re denotes the real part.

The boundary condition on the tube wall is the no-slip condition

$$\boldsymbol{u} = \frac{\partial \boldsymbol{r}'}{\partial t} \quad \text{on} \quad \mathscr{W}. \tag{2.4}$$

At $z = 0$ we apply a 'pressure' condition $p = p_{up}$. At $z = L$, we apply either another 'pressure' condition $p = p_{dn}$ or a 'flux' condition $\iint \boldsymbol{u} \cdot \hat{\boldsymbol{z}}\, \mathrm{d}A = Q_0$. (For the asymptotic calculations, the specification of a flux or a pressure at the tube end is sufficient, since we have assumed slow axial variation. Details of the conditions applied in the numerical simulations can be found in §3.3.) In both cases we define the axial velocity

scale as

$$\mathscr{U} = \frac{Q_0}{\pi a^2}, \tag{2.5}$$

where Q_0 is the steady flux through the tube in the absence of any oscillations. For the case of pressure–flux boundary conditions, Q_0 is imposed by the downstream boundary condition. For the pressure–pressure case, Q_0 must be computed by solving a steady flow problem.

This system has four dimensionless parameters:

$$St = \frac{a}{\mathscr{U}T}, \qquad \alpha^2 = \frac{\rho a^2}{\mu T}, \qquad \ell = \frac{L}{a} \qquad \text{and} \qquad \Delta. \tag{2.6a–d}$$

These are the Strouhal number (the ratio of the time scale for mean axial flow to that of the wall oscillations), the Womersley number (the ratio of the time scale for viscous diffusion to that of the oscillations), the tube aspect ratio and the dimensionless amplitude of the wall oscillations, respectively.

The results of Part 1 apply in the asymptotic regime

$$1 \ll \ell St \sim \alpha \sim \ell^2 \ll \Delta^{-1}, \tag{2.7}$$

which corresponds to a scenario in which the wall performs high-frequency small-amplitude oscillations with large axial wavelength. This regime was chosen (see §2.5 of Part 1) to include cases in which the oscillations are energetically neutral.

2.2. *Key asymptotic results from Part 1*

The main results from Part 1 are an expression for the energy transfer E from the fluid to the wall, averaged over one period of the oscillation, and the resulting condition that corresponds to $E = 0$, i.e. the point at which the oscillations are energetically neutral. The latter condition is given in the form of a critical inverse Strouhal number St_c^{-1}. Since $St^{-1} \propto \mathscr{U}$, this can be thought of as a dimensionless critical flow rate for the applied background flow. For $St^{-1} > St_c^{-1}$, i.e. at higher dimensionless flow rates, the time-averaged energy transfer E to the wall is positive.

The asymptotic predictions for E and St_c^{-1} depend only on the parameters in (2.6) and on three simple functions of the tube geometry. These are the cross-sectional area $A_0(z)$ of the steady configuration, its relative perimeter

$$\mathbb{P}(z) = \frac{1}{2(\pi A_0(z))^{1/2}} \oint_{\mathscr{C}_0(z)} \mathrm{d}s \tag{2.8}$$

and the dimensionless cross-sectional area change

$$\tilde{A}(z) = \frac{1}{a} \oint_{\mathscr{C}_0(z)} \xi \, (\hat{\boldsymbol{b}} \cdot \hat{\boldsymbol{z}})^{-1} \, \mathrm{d}s \tag{2.9}$$

induced by the oscillations. Here $\mathscr{C}_0(z)$ is the position of the tube wall surrounding a cross-section in the steady configuration and $\mathrm{d}s$ is the incremental arclength around $\mathscr{C}_0$.

From these we can compute a fourth function

$$\tilde{\mathsf{V}}(z) = \int_0^z \chi(z')\tilde{A}(z')\frac{\mathrm{d}z'}{L} - \int_z^L \left(1 - \chi(z')\right)\tilde{A}(z')\frac{\mathrm{d}z'}{L}, \tag{2.10}$$

where $\chi(z) \equiv 0$ if the flow is prescribed at the downstream end and

$$\chi(z) = \int_0^z \frac{1}{A_0(z')} \, \mathrm{d}z' \bigg/ \int_0^L \frac{1}{A_0(z')} \, \mathrm{d}z' \tag{2.11}$$

if the flow is driven by an imposed pressure drop. Physically, $\tilde{\mathbb{V}}(z)$ is the volume-flux variation at each point along the length of the tube and $\chi(z)$ is the downstream-directed fraction of the oscillatory flow generated by the wall motion at each point.

Equations (9.1) and (9.8) in Part 1 provide asymptotic predictions for E and St_c^{-1} in terms of these geometric functions. Below we provide two special cases of these predictions relevant to the scenarios considered in the current paper. Part 1 also provides asymptotic expressions for the full flow field and the other energy fluxes.

Throughout the paper, we shall present all energies on the scale

$$\mathbb{E} \equiv \rho \mathscr{U}^3 a^2 \cdot \Delta^2 \ell^2 St^3 \equiv \rho \frac{a^3 L^2}{T^3} \Delta^2, \tag{2.12}$$

which is independent of the mean velocity $\mathscr{U}$.

2.2.1. *An axially uniform steady configuration (with either set of boundary conditions)*

For a tube whose steady configuration is axially uniform with cross-sectional area $A_0 = \pi a^2$, subjected to oscillations of frequency $\omega = 2\pi/T$, Part 1 (9.1) and Part 1 (9.8) simplify to

$$E = 2\pi \mathbb{E}(|\tilde{\mathbb{V}}(0)|^2 - |\tilde{\mathbb{V}}(1)|^2) \left(\frac{1}{St} - \frac{1}{St_c} \right), \tag{2.13a}$$

$$\frac{1}{St_c} = \frac{\ell}{\alpha} \frac{2\pi^{1/2}}{|\tilde{\mathbb{V}}(0)|^2 - |\tilde{\mathbb{V}}(1)|^2} \int_0^L \mathbb{P} |\tilde{\mathbb{V}}(z)|^2 \frac{\mathrm{d}z}{L} - \Psi, \tag{2.13b}$$

where Ψ is a flux correction factor that depends on the boundary conditions at the tube ends. For pressure–flux boundary conditions we have $\Psi = 0$. With pressure–pressure boundary conditions, we have from Part 1 (9.7) that

$$\Psi = k\alpha^2 \ell \Delta^2 (|\tilde{\mathbb{V}}(0)|^2 - |\tilde{\mathbb{V}}(1)|^2), \tag{2.14}$$

where

$$k = \frac{\mu L \mathscr{U}}{a^2 (p_{up} - p_{dn})} \tag{2.15}$$

is a conductivity factor based on the geometry of the steady configuration. With a uniform tube and pressure–pressure boundary conditions, (2.11) simplifies to $\chi(z) = z/L$.

With pressure–pressure boundary conditions, Reynolds stresses generated by the oscillatory flow create an additional effective pressure gradient. This alters the steady flux Q through the tube from its value of $\pi a^2 \mathscr{U}$ in the absence of any oscillations. Including the leading-order change, Part 1 (9.6) predicts the actual steady flux to be

$$Q = \pi a^2 \mathscr{U} (1 + St \, \Psi). \tag{2.16}$$

2.2.2. *Axially non-uniform steady configuration with pressure–flux boundary conditions*

The asymptotic predictions also apply for cases in which the tube's steady configuration is axially non-uniform, which is typical of collapsible-tube systems.

For such a tube, subject to pressure–flux boundary conditions with $A_0(0) = \pi a^2$, Part 1 results (9.1) and (9.8) simplify to

$$E = 2\pi\mathbb{E}\,|\tilde{\mathbf{V}}(0)|^2 \left(\frac{1}{St} - \frac{1}{St_c}\right), \tag{2.17a}$$

$$\frac{1}{St_c} = \frac{\ell}{\alpha} \frac{2\pi^2}{|\tilde{\mathbf{V}}(0)|^2} \int_0^L \mathbb{P}(z)\, A_0(z)^{-3/2} |\tilde{\mathbf{V}}(z)|^2 \frac{\mathrm{d}z}{L}. \tag{2.17b}$$

Since $\chi \equiv 0$ with pressure–flux boundary conditions, $\tilde{\mathbf{V}}(z)$ takes the simpler form

$$\tilde{\mathbf{V}}(z) = -\int_z^L \tilde{A}(z') \frac{\mathrm{d}z'}{L}. \tag{2.18}$$

3. Three specific model problems

In the current paper, we consider three different problems that are motivated by the typical set-up in collapsible-tube experiments using a Starling resistor. We first consider the simplest realistic cases possible: a tube whose steady configuration is an axially uniform elliptical cylinder, which is subjected to oscillations of a single cross-sectional mode shape with an amplitude that varies smoothly along the length of the tube. We later relax the requirement of axial uniformity in §6.

We choose an elliptical tube because typical deformations of amplitude $O(\Delta)$ of a tube of circular cross-section result in volume changes that are $O(\Delta^2)$. This would be too small to allow a net transfer of energy to the wall to be seen in the parameter regime considered here. However, typical $O(\Delta)$ deformations of an elliptical tube (which is not too close to being circular) result in volume changes of $O(\Delta)$. (The actual area change for an ellipse with ellipticity parameter σ_0 – as introduced in §3.1 – is $O(\Delta e^{-2\sigma_0}, \Delta^2)$. The first contribution can be seen in (A 11); the second arises because of nonlinear effects. So as $\sigma_0 \to \infty$ and the ellipse becomes more circular, the $O(\Delta^2)$ area change is recovered.)

The prescribed oscillatory deformations are chosen to have zero amplitude in the two sections ($0 < z < z_1$ and $z_2 < z < L$) adjacent to each end of the tube, to mimic the rigid sections commonly used in experiments. The deformations in the central section join smoothly to the rigid sections and have an azimuthal wavenumber of 2. A sketch of the tube geometry is shown in figure 1. The specific form of the displacement field, specified below, is chosen to simplify the analysis, but we wish to stress that the general results derived in Part 1 hold for arbitrary prescribed wall displacements that induce volume changes $O(\Delta)$.

3.1. *The steady configuration for the elliptical tube*

In terms of Cartesian coordinates, the tube wall in the steady configuration is located at $\boldsymbol{r}_0 = (x, y, z)$, where

$$\frac{x}{a} = c\cosh\sigma_0\cos\check{Y}, \qquad \frac{y}{a} = c\sinh\sigma_0\sin\check{Y}, \qquad \frac{z}{L} = \check{Z}, \tag{3.1a–c}$$

in which the surface coordinates are $\check{Y} \in [0, 2\pi)$ and $\check{Z} \in [0, 1]$, c is a normalization factor, and σ_0 is an eccentricity parameter. Both σ_0 and c may be chosen to vary in z in order to obtain an axially varying steady configuration. We normalize the elliptical cross-sections by fixing $A_0(0) = \pi a^2$ and ensuring the perimeter C_0 is constant along the whole length of the tube. (The latter condition is physically realistic, since thin-walled elastic tubes deform primarily by bending rather than stretching.) For a given

$\sigma_0(z)$, we see from (A 8) and (A 9) that we should therefore take

$$c(z) = \sqrt{\frac{2}{\sinh 2\Sigma_0}} \frac{\mathrm{Ee}(\mathrm{sech}\, \Sigma_0)}{\mathrm{sech}\, \Sigma_0} \frac{\mathrm{sech}\, \sigma_0(z)}{\mathrm{Ee}(\mathrm{sech}\, \sigma_0(z))}, \tag{3.2}$$

where $\Sigma_0 = \sigma_0(0)$ and

$$\mathrm{Ee}(\kappa) \equiv \int_0^{\pi/2} (1 - \kappa^2 \sin^2 \theta)^{1/2} \, \mathrm{d}\theta \tag{3.3}$$

is the complete elliptic integral of the second kind. For an axially uniform steady configuration, (3.2) simplifies to

$$c^2 = \frac{2}{\sinh 2\sigma_0}. \tag{3.4}$$

For the axially non-uniform cases, the variation of σ_0 with z is taken to be of the form

$$\sigma_0(z) = \begin{cases} \Sigma_0 & : \quad 0 < z < z_1, \\ \Sigma_0 - \Sigma_1 \sin^2 \left(\dfrac{\pi(z - z_1)}{z_2 - z_1} \right) & : \quad z_1 < z < z_2, \\ \Sigma_0 & : \quad z_2 < z < L, \end{cases} \tag{3.5}$$

so that σ_0 varies smoothly between Σ_0 in the (axially uniform) rigid sections at each end of the tube and $\Sigma_0 - \Sigma_1$ in the centre.

3.2. *The displacement profile for the wall oscillations*

The prescribed displacement of the wall is defined in terms of the three components introduced in (2.3). We choose

$$\xi(\check{Y}, \check{Z}) = \frac{d(\check{Z}L)}{H_Y^{\mathrm{s}} H_Z^{\mathrm{s}}} \left(-\frac{3\, \mathrm{sech}\, 2\sigma_0}{4} + \cos 2\check{Y} - \frac{\mathrm{sech}\, 2\sigma_0}{4} \cos 4\check{Y} \right), \tag{3.6a}$$

$$\eta(\check{Y}, \check{Z}) = -\frac{d(\check{Z}L)}{2H_Y^{\mathrm{s}} H_Z^{\mathrm{s}}} \tanh 2\sigma_0 \, \sin 2\check{Y}, \tag{3.6b}$$

$$\zeta(\check{Y}, \check{Z}) = 0, \tag{3.6c}$$

where

$$d(z) = \begin{cases} 0 & : \quad 0 < z < z_1, \\ \sin^2 \left(\dfrac{\pi(z - z_1)}{z_2 - z_1} \right) & : \quad z_1 < z < z_2, \\ 0 & : \quad z_2 < z < L, \end{cases} \tag{3.7}$$

is the smoothly varying amplitude function and $H_Y^{\mathrm{s}}(\check{Y}, \check{Z})$ and $H_Z^{\mathrm{s}}(\check{Y}, \check{Z})$ are the surface scale factors defined in Part 1 (2.4). In general, we have

$$H_Y^{\mathrm{s}} = c \left(\frac{\cosh 2\sigma_0 - \cos 2\check{Y}}{2} \right)^{1/2}, \qquad H_Z^{\mathrm{s}} = \frac{1}{\hat{z} \cdot \hat{b}}. \tag{3.8a,b}$$

For an axially uniform tube, we have

$$H_Y^{\mathrm{s}} = \left(\frac{\cosh 2\sigma_0 - \cos 2\check{Y}}{\sinh 2\sigma_0} \right)^{1/2}, \qquad H_Z^{\mathrm{s}} = 1. \tag{3.9a,b}$$

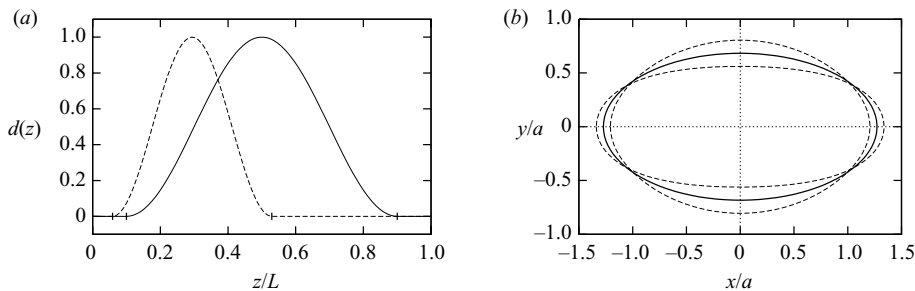The deformations are depicted in figure 2.

FIGURE 2. The prescribed deformations applied to the tube. (*a*) The axial amplitude function $d(z)$ from (3.7) for the cases $z_1 = L/10$, $z_2 = 9L/10$ (solid line) used for the pressure–flux case of §4 and $z_1 = L/17$, $z_2 = 9L/17$ (dashed line) used for the pressure–pressure case of §5. (*b*) The initial elliptical cross-section for $\sigma_0 = 0.6$ (solid line), together with the extremal deformations (3.6) with exaggerated amplitude $\Delta = 0.1$ (dashed line).

An explanation of the chosen form (3.6)–(3.7) is in order. The factor $H_{\check{Y}}^s H_{\check{Z}}^s$ is introduced in (3.6) because it is convenient when it comes to solving the fluid problem and also when computing the changes $\tilde{A}$ in the cross-sectional area (see (2.9)). The remaining dependence on the azimuthal coordinate $\check{Y}$ is then conveniently expressed using Fourier-like terms of the form $a_n \cos(2n\check{Y})$ for ξ and $b_n \sin(2n\check{Y})$ for η. (In the expansion for ξ, only the $n = 0$ term leads to a change in the cross-sectional area at leading order in Δ.) The relative coefficients of these terms were chosen so as to conserve circumferential length at leading order. Conveniently, we find that this condition can be satisfied with a small number of terms, and the resulting displacement field has an azimuthal wavenumber of 2.

Observe that in the limit $\sigma_0 \to \infty$, the steady configuration approaches a circular cross-section, and the deformations take a somewhat simpler form. However, there is then no change in the cross-sectional area at leading order.

3.3. *Solution methods*

We simulated the flow in the oscillating tube, using the object-oriented multi-physics finite-element library `oomph-lib` (Heil & Hazel 2006) to solve the three-dimensional unsteady Navier–Stokes equations (2.1) in the moving domain (the tube with the prescribed wall motion) specified in §§ 2, 3.1 and 3.2. The flow was driven either by prescribing the axial velocity profile at the downstream end, leaving the inflow axially traction-free (the 'pressure–flux' boundary conditions), or by imposing a pressure drop between the upstream and downstream ends, such that in the absence of any wall motion the flow is steady Poiseuille flow with uniform flux $\pi a^2 \mathscr{U}$ (the 'pressure–pressure' boundary conditions). We exploited the symmetry of the configuration and discretized only one quarter of the domain, applying appropriate symmetry conditions in the planes $x = 0$ and $y = 0$. Details of the numerical scheme and code validation can be found in Heil & Waters (2008), in which computations were performed using the same code.

We compare the numerical results with the asymptotic predictions for E and St_c^{-1} given in § 2.2. We also use the methods described in Part 1 to calculate the first few terms of the asymptotic expansions for the velocity and pressure fields inside the tube and compare these with the numerical results. Full details of the relevant calculations and the evaluation of the integrals for E and St_c^{-1} can be found in Appendices A–D.

The asymptotic calculations of Part 1 assume that the flow is periodic; so we must ensure that the numerical simulations have reached such a state before attempting

any comparisons. For simplicity, the initial conditions used in the simulations were a uniform Poiseuille flow in each cross-section of the steady configuration. This does not satisfy the boundary conditions on the moving wall, but the velocity field quickly adjusts to take account of this over the first few time steps. In the case of pressure–flux boundary conditions, the system is found to quickly settle down to a periodic state. For pressure–pressure boundary conditions, the relaxation to a periodic state takes longer, through a slow adjustment of the background flux about which the system oscillates. (With pressure–flux boundary conditions this mode is absent, since the flux is fixed by the condition at the downstream end.) This adjustment is discussed in detail in §5.2.

4. An axially uniform tube with pressure–flux boundary conditions

We start by considering a case in which the flow is driven by an imposed flow at the downstream end of the tube and is subject to a fixed pressure at the upstream end. Calculations were performed with $\sigma_0 = 0.6$ (corresponding to an elliptical cross-section with semi-axes of 1.365 and 0.733), $z_1 = 0.1\,L$ and $z_2 = 0.9\,L$ and $\Delta = 0.025$. Simulations were then performed for various values of α, ℓ and St, corresponding, for example, to variations in μ, L and $\mathcal{U}$. The numerical results will be compared with the energy flux results (2.13) and also with the full flow fields calculated in Appendix B.

4.1. *Velocity and pressure fields*

Figure 3 illustrates the numerically computed axial velocity profiles for $\alpha^2 = 100$, $\ell = 10$ and $St^{-1} = 1.5$, at quarter-period intervals. In each case, the upper figure shows the total axial velocity w, while the lower figure shows the (magnified) perturbation to the steady mean flow, obtained by subtracting the Poiseuille flow profile (B 6) from w. The flow exhibits the expected structure: a mean Poiseuille flow plus an oscillatory component driven by the wall motion. The oscillatory flow is almost uniform over most of the cross-section, with a thin Stokes layer adjacent to the wall.

Figure 4 shows a direct comparison between the numerical results (dashed lines) and asymptotic predictions (solid lines) for the axial velocity w and pressure p along the centreline $x = y = 0$ of the tube at the same four instants as in figure 3.

The plot of the centreline velocity $w(0, 0, z; t)$ in figure 4(a) illustrates how the magnitude of the axial velocity perturbation increases towards the upstream end of the tube. At the far downstream end of the tube, the prescribed Poiseuille flow profile imposes a constant value $w(0, 0, L; t) = 2\mathcal{U}$. When the tube becomes more collapsed, the volume of the cross-sectional slices in the central deforming part of the tube decreases, and some of the fluid occupying these slices must be displaced. Since the flow rate is held constant at the downstream end, the fluid can only be displaced towards the upstream end of the tube. As the wall moves inwards (e.g. at $t = 4.75\,T$), each infinitesimal cross-sectional 'slice' therefore makes a small negative contribution to the volume flux upstream of its position. As the wall moves outwards (e.g. at $t = 4.25\,T$) the same applies, but the contributions are positive. At each position along the tube the fluctuations in flux are precisely due to the volume change occurring downstream of that position. Since, for the mode-1 oscillations considered here, the changes to the cross-sectional area at different axial positions are all in phase with each other, the fluctuations are maximal at the upstream end.

We also observe in figure 4(a) that the perturbation to the centreline velocity is slightly out of phase with the volume flux changes caused by the wall motion. In
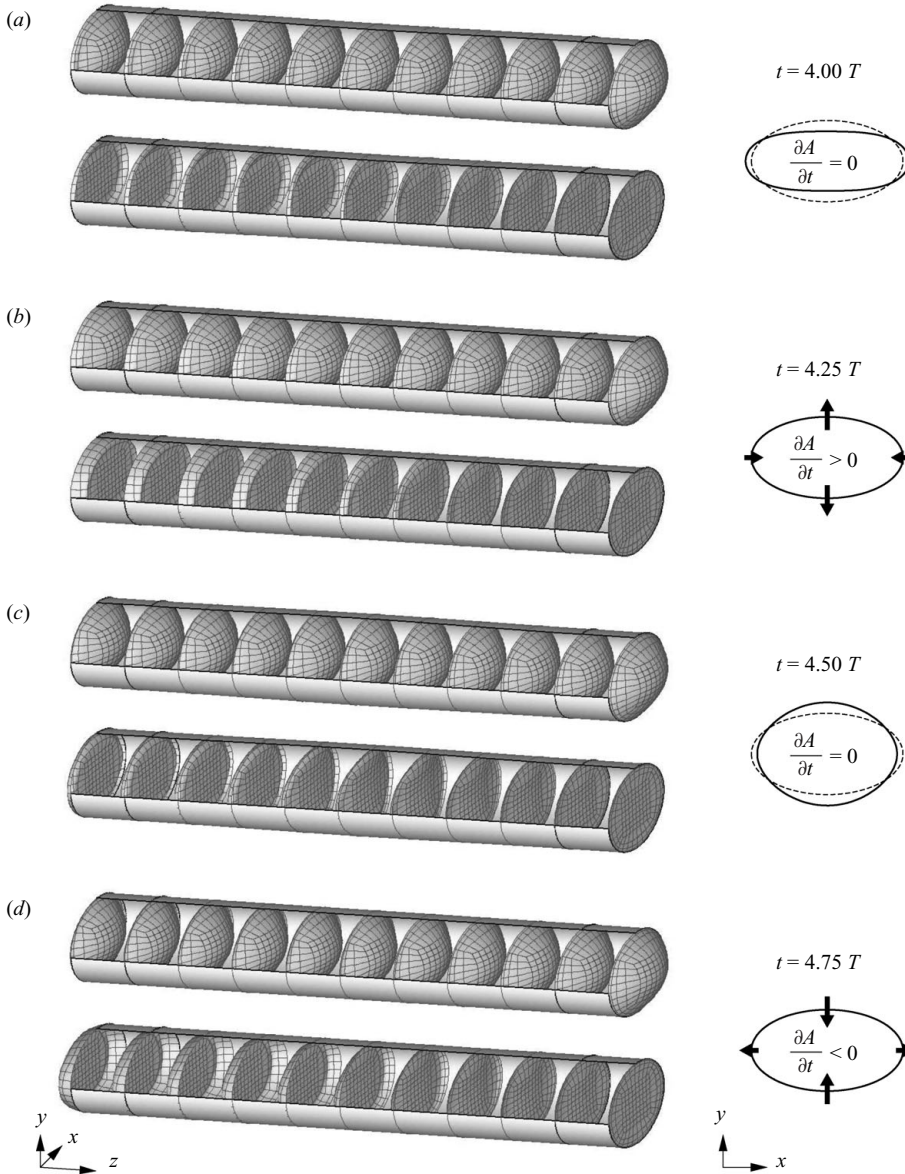
FIGURE 3. Numerical results at four equally spaced instants during the fifth period of the oscillation for $\alpha^2 = 100$, $St^{-1} = 1.5$, $\Delta = 0.025$, $\ell = 10$, $z_1 = 0.1\,L$, $z_2 = 0.9\,L$, with the prescribed wall motion described in §3.2 and an imposed steady Poiseuille flow at the downstream (right-hand) end. Left: profiles of the axial velocity at each instant. The upper plot in each part shows the full axial velocity profile w, while the lower one shows the perturbation obtained by subtracting the Poiseuille profile (B6) from w. The perturbation velocities are magnified by a factor of 3 for visualization purposes. Right: an exaggerated depiction of the tube cross-section at each instant. The dashed ellipse is the steady configuration, and the arrows indicate instantaneous velocities of the wall. In (a) and (c) the wall is in its extremal configurations and so is instantaneously at rest.

particular, w is not exactly $2\mathcal{U}$ at $t = 4.0\,T$ and $t = 4.5\,T$ when the wall is at rest. This is consistent with the asymptotic predictions (B9) and (B21). The leading-order oscillatory velocity ($\tilde{w}_{00}$ in the notation of Part 1) is in phase with the wall velocity,
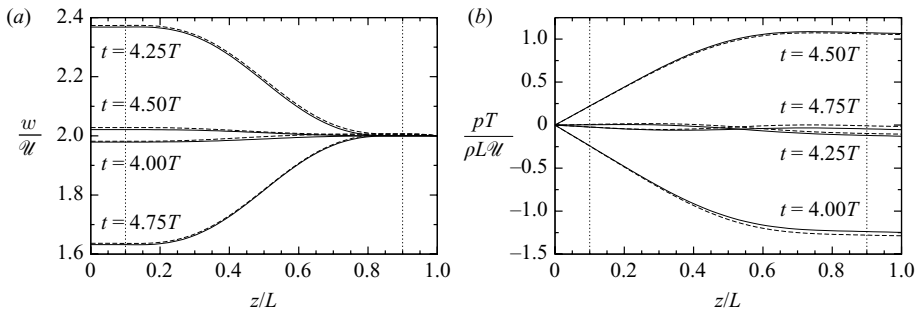
FIGURE 4. Plots of (*a*) the centreline axial velocity $w(0, 0, z; t)$ and (*b*) the centreline pressure $p(0, 0, z; t)$ at four equally spaced instants of the oscillation for the same set-up and parameter values as in figure 3. The solid lines denote the asymptotic prediction (B 26) and (B 22); the dashed lines denote numerical results. The dotted vertical lines show the boundary between the rigid and flexible sections at $z = z_1$ and $z = z_2$.

but there are out-of-phase corrections at $O(\alpha^{-1})$ because of viscous effects in the Stokes layer (and these appear in $\tilde{w}_{01}$ as the term involving C_0/R).

Viscosity acts in the oscillatory Stokes layer, which, like a classical Womersley layer, contains a velocity component that is out of phase with the wall motion (see (B 18)). The non-zero axial perturbation velocities in the Stokes layer at instants when the wall is at rest are clearly visible in figure 3(*a*,*c*). The non-zero oscillatory axial volume flux generated in these layers must be compensated for by an additional small oscillatory axial velocity in the core region to achieve the required total volume flux set by global mass conservation.

The plot of the centreline pressure $p(0, 0, z; t)$ in figure 4(*b*) indicates that the pressure distribution is dominated by the large axial pressure gradients required to accelerate and decelerate the flow during the high-frequency oscillations. The viscous pressure drop associated with the steady mean flow is much smaller than these inertial pressure fluctuations. The pressure is not exactly in phase with the accelerations of the wall, for the same reasons (viscous effects in the Stokes layer, as discussed above) that the axial velocity is not exactly in phase with the velocity of the wall.

Figure 5 shows a direct comparison between the numerical (right) and asymptotic (left) predictions for the velocity and pressure distributions in the cross-sectional plane $z = 0.5 L$ at $t = 4.875 T$ (i.e. 7/8th through a period of the oscillation). At this instant of time, the wall still collapses inwards but decelerates as it approaches its most strongly deformed configuration. The upper two plots show contours of pressure p and instantaneous streamlines of the transverse velocity $\boldsymbol{u}^{\perp}$. The transverse velocity field is dominated by the stagnation-point-like core flow, while the boundary layers remain passive. The transverse flow is decelerated by an adverse pressure gradient, but the induced cross-sectional pressure variations are small compared with the pressure variations along the tube, shown in figure 4(*b*).

The lower two plots in figure 5 show the axial velocity profile in the same cross-section and illustrate how the Poiseuille flow profile is depleted by the upstream-directed axial velocity perturbation: the centreline velocity is reduced slightly below the Poiseuille value of $2\mathcal{U}$, and the effect of the Stokes layer on the velocity distribution is clearly visible in both plots.
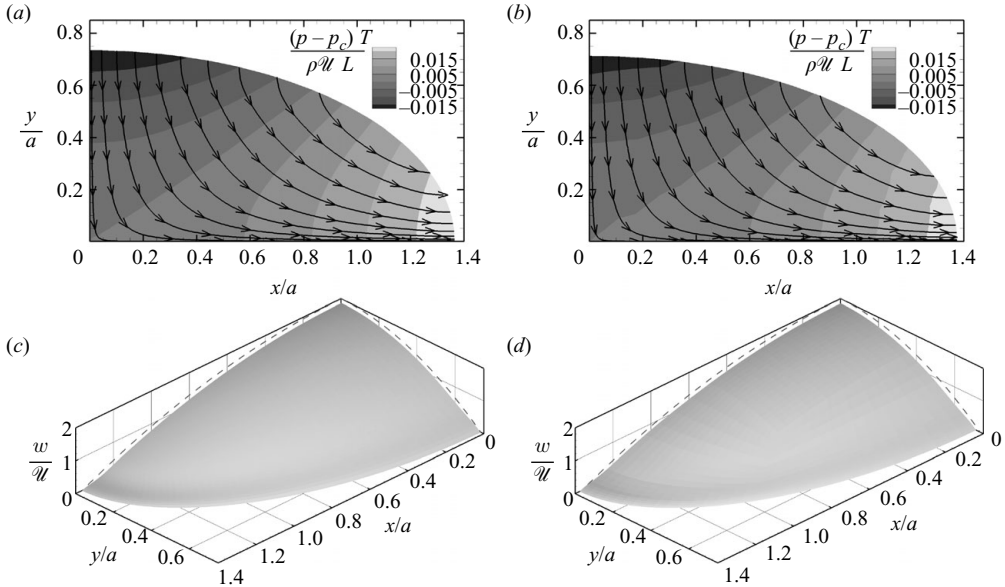
FIGURE 5. Comparison of the (a,c) asymptotic and (b,d) numerical predictions for the flow field in a cross-sectional slice at $z = 0.5\,L$, at $t = 4.875\,T$, with the same set-up and parameter values as in figure 3. Only one quarter of each cross-section is shown. (a,b) Instantaneous streamlines of the transverse velocity $\boldsymbol{u}^\perp$ and contours of the pressure $p - p_c$ relative to the centreline pressure p_c. (c,d) Profiles of the axial velocity w. The asymptotic results are taken from the composite expansions in §B.6. The dashed lines in (c,d) show the steady Poiseuille flow that would occur in the absence of any oscillations.

4.2. *Energy budget and criticality condition*

Figure 6 illustrates the system's energy budget. The work done by the fluid on the wall is given by

$$W(t) = \int_0^t \iint_{\mathscr{W}} \boldsymbol{u} \cdot \left(p\boldsymbol{I} - 2\mu\boldsymbol{e}\right) \cdot \hat{\boldsymbol{N}}\,\mathrm{d}S\,\mathrm{d}t', \tag{4.1}$$

where $\hat{\boldsymbol{N}}$ is the outward-pointing unit normal to the moving wall $\mathscr{W}(t)$, $\boldsymbol{I}$ is the identity tensor, and $\boldsymbol{e}$ is the rate-of-strain tensor. The mean rate of working, E, is found by averaging $\mathrm{d}W/\mathrm{d}t$ over a period of the oscillation:

$$E = \frac{W(t^* + T) - W(t^*)}{T} = \frac{1}{T}\int_{t^*}^{t^*+T} \iint_{\mathscr{W}} \boldsymbol{u} \cdot \left(p\boldsymbol{I} - 2\mu\boldsymbol{e}\right) \cdot \hat{\boldsymbol{N}}\,\mathrm{d}S\,\mathrm{d}t, \tag{4.2}$$

where t^* is taken to be sufficiently large so that the system has settled into a periodic state.

Figure 6(a) shows a plot of $W(t)$ for several different inverse Strouhal numbers. As can be seen, there are certain time intervals in the period of the motion in which the wall does work on the fluid and others in which the fluid does work on the wall. The oscillations in the work are dominated by oscillation of period $T/2$ caused by the product of the oscillatory period-T components of the pressure p and velocity $\boldsymbol{u}$. A smaller component with period T arises from the product of the steady pressure and the oscillatory component of the velocity.

We observe from (B 18a) and (B 10) that the leading-order oscillatory normal velocity and pressure are proportional to $\sin(2\pi t/T)$ and $-\cos(2\pi t/T)$ respectively,
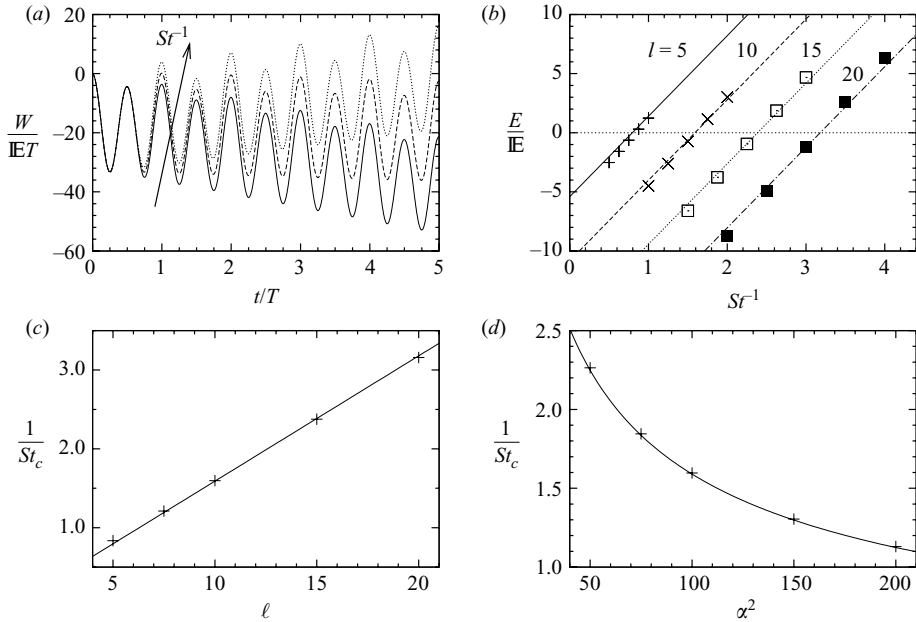
FIGURE 6. Energy budget comparisons for pressure–flux boundary conditions. (*a*) Numerical evolution of the total work $W(t)$ done by the fluid on the wall for $\alpha^2 = 100$ and $\ell = 10$, with $St^{-1} = 1.0$ (solid line), 1.5 (dashed line), 2.0 (dotted line). (*b*) Mean energy flux E from the fluid to the wall as a function of St^{-1}, at $\alpha^2 = 100$ and with various tube lengths ℓ. (*c*) The critical inverse Strouhal number St_c^{-1} as a function of ℓ at $\alpha^2 = 100$. (*d*) St_c^{-1} as a function of α^2, for $\ell = 10$. Other parameters as in figure 3. In (*b*)–(*d*), the points denote numerical results; the lines denote the asymptotic predictions (4.3) and (4.4).

while from (B 8) the steady pressure component is negative. Inserting these forms into (4.1) we find that the period-$T/2$ component of W is proportional to $\cos(4\pi t/T)$, while the (smaller) period-T component is proportional to $\cos(2\pi t/T)$. This is consistent with the oscillations in figure 6(*a*).

On top of these oscillations is a general increasing or decreasing trend, growing linearly with time. At lower St^{-1} (lower flow rates) the wall, on average, does more work on the fluid over a period of the motion. This implies that the oscillation can only be maintained if an external agency provides that energy to the wall. Our conjecture is that in a fully coupled fluid–structure interaction problem in which the wall is allowed to move freely and no external input of energy to the wall is available, the oscillations would decay. As St^{-1} is increased, the average work done by the fluid on the wall over a period increases. At $St^{-1} \approx 1.59$ (for these particular parameter values) the oscillation becomes energetically neutral over a period. For higher St^{-1} (corresponding, e.g., to higher background flows $\mathscr{U}$) the wall extracts energy from the flow. We conjecture that this would be a necessary condition for oscillations to grow in the corresponding fluid–structure interaction problem.

Figure 6(*b*) summarizes these results, by showing E as a function of the inverse Strouhal number St^{-1}. The different sets of results correspond to different tube lengths ℓ. An asymptotic estimate for E is provided by the result (2.17). The detailed calculation for the specific problem set-up and tube geometry used here is presented
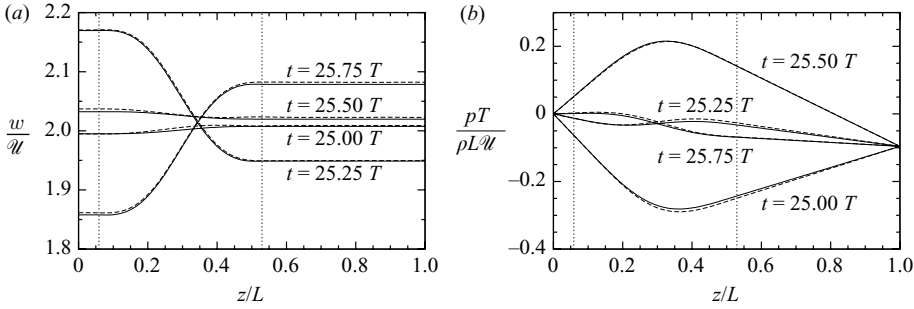
FIGURE 7. Plots of (*a*) the centreline axial velocity $w(0,0,z;t)$ and (*b*) the centreline pressure $p(0,0,z;t)$ at four equally spaced instants of the oscillation with pressure–pressure boundary conditions. The set-up is as described at the beginning of §5, with $\alpha^2 = 100$ and $St^{-1} = 2.5$. The solid lines are the asymptotic predictions (calculations omitted for brevity), and the dashed lines represent the numerical results. The dotted vertical lines show the boundary between the rigid and flexible sections at $z = z_1$ and $z = z_2$.

in §B.1. From (B 2) and (B 3), we obtain

$$E \sim 6.81 \, \mathbb{E} \left(\frac{1}{St} - \frac{1}{St_c} \right), \qquad (4.3)$$

where

$$\frac{1}{St_c} \sim \frac{1.59\,\ell}{\alpha} \qquad (4.4)$$

is the critical inverse Strouhal number at which the oscillations are energetically neutral. The numerical results are seen to be in excellent agreement with these predictions.

Figure 6(*c,d*) confirms the accuracy of (4.4), by comparing the predicted behaviour of St_c^{-1} with numerical results for varying α and ℓ. We see that within the parameter regime considered here, shorter tubes are capable of extracting energy from the mean flow at smaller flow rates and that an increase in the Womersley number α^2 (e.g. via a reduction in the fluid viscosity while keeping all other parameters constant) also reduces the dimensionless flow rate beyond which energy is transferred from the flow to the wall.

5. An axially uniform tube with pressure–pressure conditions

Next we consider the case in which the flow is driven by a prescribed pressure drop between the far-upstream and downstream ends of the system. Since the instability mechanism considered here requires the fluctuations in kinetic energy at the inflow to exceed those at the outflow, we break the system's upstream–downstream symmetry by making the rigid downstream tube longer than its upstream counterpart, setting $z_1 = L/17$ and $z_2 = 9L/17$. Throughout this section we use $\ell \equiv L/a = 17$ and $\sigma_0 = 0.6$ as in the pressure–flux case.

5.1. *Velocity and pressure fields*

Figure 7 illustrates the axial velocity and pressure on the tube's centreline at four equally spaced instants during a period of the oscillation, for $\alpha^2 = 100$ and $St^{-1} = 2.5$. The numerical and asymptotic results are in excellent agreement.

At the beginning of the period (at $t = 25\,T$), the tube wall is in its most strongly collapsed configuration. The wall is instantaneously at rest and does not drive any axial sloshing flow. The centreline velocity is therefore close to, but is not precisely, its mean value. The deviation occurs for the same reasons as in the pressure–flux case (see the discussion in §4.1). However, for the pressure–pressure case, the mean value is a little greater than $2\mathscr{U}$, since the oscillations increase the mean flux slightly (see §7 of Part 1 and §5.2 of the current paper).

Strong axial pressure gradients act in the upstream and downstream rigid sections and accelerate the fluid, so that after a quarter of the period, at $t = 25.25\,T$, when the wall has returned to its steady configuration and is moving at maximum velocity, strong sloshing flows are driven from the central section into the upstream and downstream rigid sections. Upstream, the sloshing flow acts against the direction of the mean flow, leading to a reduction in centreline velocity, while downstream it augments the mean flow. At this instant, there is little net acceleration of the fluid; hence the axial pressure variation is dominated by the imposed pressure drop, applied between the far-upstream and downstream ends.

During the second half of the cycle the pattern reverses. Strong axial pressure gradients in the upstream and downstream rigid tubes decelerate the sloshing flows until they (approximately) disappear when the tube wall comes to rest in its second extreme configuration. As in the case of the pressure–flux boundary conditions, viscosity, acting in the Stokes layers, induces small phase differences between the wall motion and the fluid motion in the core region.

5.2. *The slow adjustment of the mean flow*

When analysing the energy budget for the numerical simulations with pressure–flux boundary conditions, we computed the average work done E by the fluid on the wall over a few periods of the oscillation around $t = 5T$. This straightforward computation was appropriate because the prescribed flow rate at the far downstream end ensured that the system settled quickly into a periodic steady state, allowing the averaging to be performed after a few periods of the oscillation.

With pressure–pressure boundary conditions this is no longer the case because following the impulsive start of the wall oscillation at $t = 0$, the mean flux through the system (as computed by averaging over a period T of the wall motion) adjusts slowly over a time scale that is much larger than the period T of the oscillation. After some initial transients, the adjustment towards the long-time limiting value is well described by a decaying exponential, as shown in figure 8. There, the initial transients occupy the first 10 or so periods, with the exponential fit being a good approximation for $t \gtrsim 10T$.

The deviation of the mean flow from its long-time steady limit is the result of two effects. Firstly, the initial condition imposes an initial flux of $\pi a^2 \mathscr{U}$, the value we would obtain with the applied pressure drop in the absence of any oscillation. However, as discussed in §7 of Part 1 and §5.3 of the present paper, the presence of the oscillations increases this flux through the action of Reynolds stresses. Secondly, initial transients, caused by the impulsive start from the steady initial conditions (see §3.3), mean that the volume flux averaged over (say) the second period of the motion is significantly different from that imposed at $t = 0$. In many of the simulations it is this second effect that creates the larger deviation from the limiting value of the steady flux. This explains, for example, why the average of the axial flux over each period is seen to decrease (rather than increase) towards its final value in figure 8(*a*).
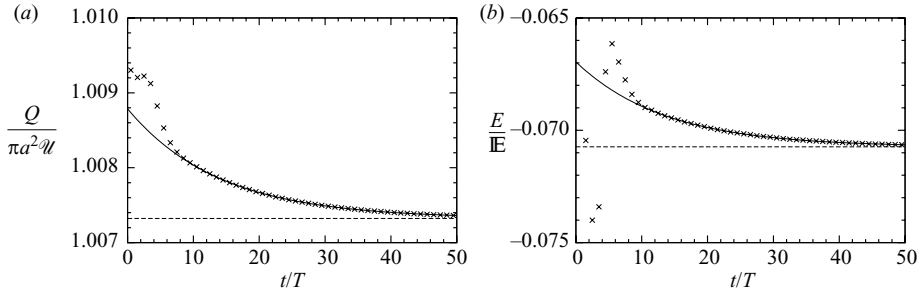
FIGURE 8. An illustration of the initial transients and the slow adjustment of the system to a periodic state, for (a) the mean axial volume flux and (b) the mean rate of working by the fluid on the wall. The points are numerical data from a simulation with $\alpha^2 = 100$, $St^{-1} = 2.5$ and other parameters as given at the beginning of §5. Each point is the average value taken over one period T of the oscillations. The continuous lines are functions of the form $A + Be^{-\lambda t}$. Initial transients occupy $0 \leqslant t/T \lesssim 10$, and the parameters A, B and λ were found using a least squares fit to the numerical data for $10 < t/T < 50$. The dashed lines are the asymptotes of the fitted functions as $t \to \infty$.

The limiting value of the steady flux is determined by a balance between the effective axial pressure gradient (the imposed gradient plus the Reynolds stresses from the oscillatory flow) and viscous stresses. We conjecture that after the initial transients, the adjustment towards the limiting value is regulated by an axially uniform axial acceleration of the body of fluid contained in the tube under the forces that arise from the mismatch of the effective pressure and viscous forces. (This assumption is justified *a posteriori* by the excellent agreement – as shown in figures 8 and 9a – between the numerical simulations and the analysis that now follows.)

The effective pressure gradient necessarily scales like the viscous forces, since the two must balance in steady state. We therefore estimate the time scale of the adjustment by balancing the unsteady inertia term $\rho\, \partial w/\partial t$ with the viscous dissipation $\mu \nabla^2 w$ of the axial flow. From this balance we obtain the time scale

$$T_i \sim \frac{a^2 \rho}{\mu} = \alpha^2 T. \qquad (5.1)$$

Since $\alpha^2 \gg 1$, the time scale T_i is much longer than the period T of the wall motion, consistent with the observed behaviour in the numerical simulations. We therefore examine the slow adjustment using a multiple-scale analysis. We start by defining a slow time $t^* = t/T_i$ in addition to the (fast) non-dimensional time $\check{t} = t/T$ appropriate to the oscillations. We then decompose the axial velocity as

$$w(\boldsymbol{x}, t) = \mathscr{U}\left[\left(\overline{w}(\boldsymbol{x}) + \overline{w}^*(\boldsymbol{x}, t^*)\right) + \left(\tilde{w}(\boldsymbol{x}) + \tilde{w}^*(\boldsymbol{x}, t^*)\right) e^{2\pi i \check{t}} + \cdots \right], \qquad (5.2)$$

where $\overline{w}$ and $\tilde{w}$ are the steady and frequency-ω components in the converged purely oscillatory state. The other variables are decomposed similarly. Using the slow time t^*, the time derivative becomes

$$\frac{\partial}{\partial t} = \frac{1}{T}\left(\frac{1}{\alpha^2} \frac{\partial}{\partial t^*} + \frac{\partial}{\partial \check{t}} \right). \qquad (5.3)$$

We now substitute this decomposition into the Navier–Stokes equations (2.1) and average over a period T of the fast oscillations. Using the fact that $\overline{w}$, $\tilde{w}$ and the like satisfy the equations when $\partial/\partial t^* = 0$, and assuming $\overline{w}^*$, $\tilde{w}^*$ and the like are
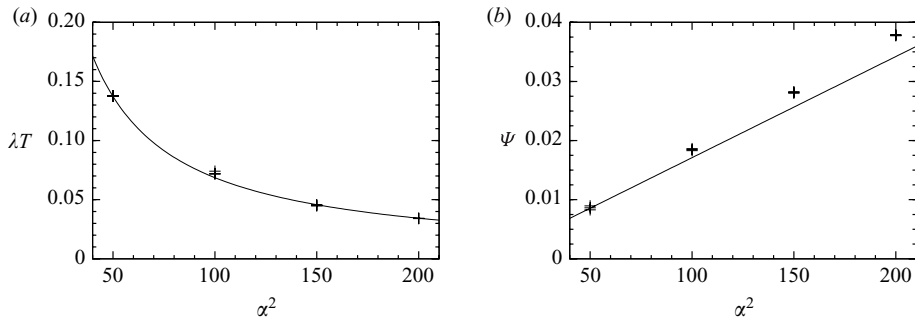
FIGURE 9. (*a*) The decay constants λ for the adjustment of the mean flux. The solid line is the theoretical prediction $\lambda = 6.864/(\alpha^2 T)$. The points indicate results from the numerical simulations, found by fitting the exponential form $A + B\mathrm{e}^{-\lambda t}$ to a moving average taken over a window of length T. (*b*) The flux correction factor Ψ as a function of the Womersley number α. The points represent numerical results, where Ψ is computed from the flux Q using (5.7). The line is the theoretical prediction (5.8). For both graphs, for each value of α, simulations were run with three different values of St (see figure 10*a*). The three points for each α are almost indistinguishable on the graphs, consistent with the theoretical predictions that λ and Ψ are independent of St.

independent of z, we obtain

$$\frac{\partial \bar{w}^*}{\partial t^*} = \check{\nabla}_\perp^2 \bar{w}^*. \tag{5.4}$$

at leading order, where $\check{\nabla}_\perp^2 \equiv a^2 \nabla_\perp^2$ is the dimensionless cross-sectional Laplacian. The boundary conditions are that $\bar{w}^* = 0$ on the tube wall, linearized to the steady configuration of an elliptical cylinder. Equation (5.4) represents the decay of a flow in a tube from a non-zero initial state under zero pressure gradient. We can analyse this adjustment theoretically, following e.g. Mortensen & Bruus (2006).

The solutions of (5.4) can be written as

$$\bar{w}^*(\check{x}, \check{y}, t^*) = \sum_n k_n \, \Phi_n(\check{x}, \check{y}) \, \mathrm{e}^{-\lambda_n^* t^*}, \tag{5.5}$$

where Φ_n and λ_n^* are the eigenfunctions and eigenvalues of the Helmholtz problem

$$\check{\nabla}_\perp^2 \Phi_n = \lambda_n^* \Phi_n \tag{5.6}$$

in the elliptical cross-section, subject to $\Phi_n = 0$ on the boundary, and k_n are constants set by the initial conditions.

The long-time behaviour of the decay towards the steady state is therefore controlled by the smallest eigenvalue λ_0^*. We evaluate this, for our ellipse of $\sigma_0 = 0.6$, using the polynomial approximation of Troesch & Troesch (1973). We obtain $\lambda_0^* = 6.864$. Figure 9(*a*) shows that the decay observed in the numerical simulations is in excellent agreement with the theoretical (dimensional) decay constant $\lambda = \lambda_0^*/(\alpha^2 T)$.

At large Womersley numbers, the rate at which the mean flux approaches its asymptotic value is therefore very slow relative to the period of the oscillations, and it is infeasible to continue the numerical simulations long enough to obtain complete convergence. For instance, for $\alpha^2 = 200$ and $St^{-1} = 1.75$ the rate-of-work E done by the wall, averaged over the 50th period of the oscillation, still differs by more than 20 % from its asymptotic value. However, since the decay is so well approximated by an exponential, we shall use a least-squares fit to such a function to determine the

asymptotic values of the various quantities of interest when analysing the system's energy budget in § 5.4.

5.3. *The oscillation-induced flux correction*

As described in § 7 of Part 1, the oscillatory flow can affect the steady component of the momentum equation via the time average of the nonlinear momentum term. The resulting Reynolds stresses act like an additional pressure gradient on the steady flow. In the case of pressure–flux boundary conditions, the steady pressure field can adjust without affecting the axial volume flux. With pressure–pressure boundary conditions the axial volume flux must change from the value $\pi a^2 \mathscr{U}$ that would be obtained in the absence of any oscillations.

This change is parameterized by a flux correction factor Ψ, with the observed steady flux (following the adjustment described in § 5.2 above) being written as

$$Q = \pi a^2 \mathscr{U}(1 + St\,\Psi). \tag{5.7}$$

The asymptotic prediction for Ψ from Part 1 for a tube with an axially uniform steady configuration is given in (2.16). We have that $\Psi > 0$ whenever the oscillation volume $\mathbb{V}$ is larger at the upstream end than at the downstream end. (The condition $|\mathbb{V}(0)| > |\mathbb{V}(L)|$ is a prerequisite for the extraction of energy from the mean flow and is satisfied in each of the numerical simulations described here.) For the cases considered here, (C 3) predicts

$$\Psi = 0.0161\alpha^2\Delta^2\ell. \tag{5.8}$$

Estimates of Ψ can be obtained from the numerical simulations using the asymptotic value of Q obtained from the least squares fit discussed in § 5.2 and the expression (5.7). Figure 9(b) shows a comparison between these numerical results and the theoretical prediction (5.8). The agreement is good, though somewhat counter-intuitively, the agreement appears to get worse as α increases. However, a closer analysis of the relative errors in Ψ shows them to be well approximated by a function of the form $f(St, \ell) - C\alpha^{-1}$, for some function f and constant C. This is consistent with the prediction being asymptotic as $\alpha, \ell, St \to \infty$. The better agreement at $\alpha^2 = 50$ is probably because of a coincidental cancellation between $f(St, \ell)$ and $C\alpha^{-1}$ there.

5.4. *The energy budget and critical inverse Strouhal number*

Asymptotic predictions for the net energy transfer to the wall E and the critical Strouhal number St_c are given by (2.13). The detailed calculations for the specific set-up considered in this section can be found in Appendix C. Substituting $z_1 = L/17$ $z_2 = 9L/17$, $\sigma_0 = 0.6$, $\omega = 2\pi/T$ into (C 4) and (C 5), we find that

$$E \sim 0.97\,\mathbb{E}\left(\frac{1}{St} - \frac{1}{St_c}\right) \tag{5.9}$$

and

$$\frac{1}{St_c} \sim \frac{1.47\,\ell}{\alpha} - 0.0161\,\alpha^2\Delta^2\ell. \tag{5.10}$$

The second term on the right-hand side of (5.10) is due to the change in the mean axial volume flux caused by the oscillations. The higher mean flux enhances the net oscillatory kinetic energy flux at the tube ends, resulting in a greater flux of kinetic energy into the system. The larger volume flux therefore has the effect of increasing the energy transfer to the wall and thus reducing the critical inverse Strouhal number.
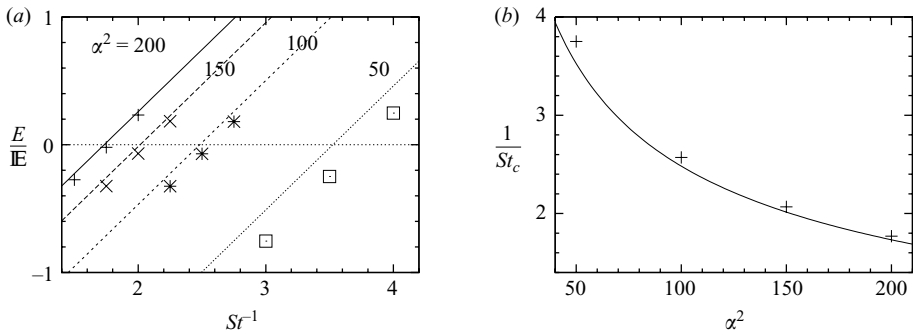
FIGURE 10. Comparison of the numerical and asymptotic results for pressure–pressure boundary conditions with $\sigma_0 = 0.6$, $z_1 = L/17$, $z_2 = 9L/17$, $\ell = 17$. (a) The net energy transfer to the wall as a function of St^{-1} for various α^2. (b) The critical inverse Strouhal number St_c^{-1} as a function of Womersley number α^2. Results from numerical simulations are shown with the points and the asymptotic results (5.9) and (5.10) with the continuous lines.

Figure 10(a) shows a comparison between the numerical and asymptotic predictions for the time-averaged work E done by the fluid on the wall, as a function of St^{-1}, for various values of α^2. The overall behaviour is similar to that found in the case of pressure–flux boundary conditions: for fixed α^2, the rate-of-work E done by the fluid on the wall increases with the flow rate (represented by the St^{-1}), and St_c^{-1} decreases with an increase in α^2. The agreement between numerical and asymptotic predictions in figure 10 is slightly worse than in the case of pressure–flux boundary conditions (figure 6b, d). However, the agreement improves as the Womersley number is increased, as expected.

The asymptotic predictions are not quite as good for the pressure–pressure case, probably because the net energy flux at the tube ends is now the difference between that at the upstream and downstream ends. A small error in the partitioning of the mass flux from the prescribed volume changes in the tube will cause an error of the same sign at both ends of the tube. This source of error is absent in the pressure–flux case, since only one end contributes to each flux.

6. An axially non-uniform tube with pressure–flux conditions

Finally, we consider a tube in which the steady configuration is not axially uniform, choosing the ellipticity σ_0 of each cross-section in the steady configuration to vary with z, as described in (3.5). For simplicity, we consider only pressure–flux boundary conditions, and take $\Sigma_0 = 0.6$ so that the rigid end sections of the tube have the same cross-section as those in §§ 4 and 5.

Figure 11(a) illustrates the axial non-uniformity of the tube: the solid line shows the cross-sections of the rigid upstream and downstream tubes, while the various dashed lines show the most strongly collapsed cross-sections at the centre of the 'elastic' section for a range of axial non-uniformities, characterized by the parameter Σ_1 in (3.5).

The calculations to obtain the asymptotic expressions for the energy transfer to the wall and the critical inverse Strouhal number are described in Appendix D.
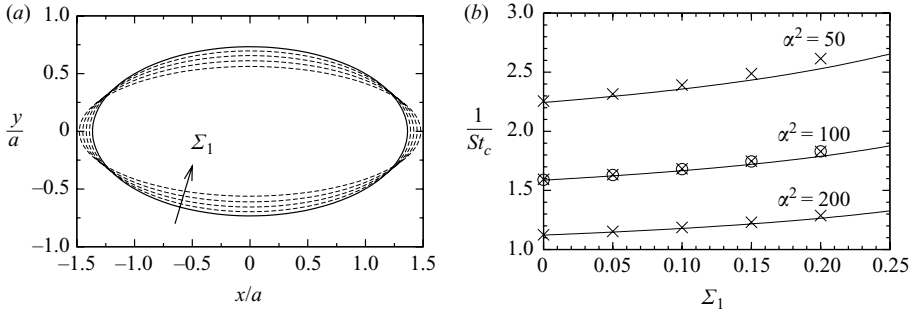
FIGURE 11. (*a*) Elliptical cross-sections in the axially non-uniform steady configuration as described in §3.1 with $\Sigma_0 = 0.6$. The solid line is the cross-section of the rigid end sections. The dashed lines are the cross-section of the most collapsed part at $z = (z_1 + z_2)/2$ for $\Sigma_1 = 0.05, 0.10, 0.15, 0.20$ ($\Sigma_1 = 0$ corresponds to an axially uniform steady configuration). (*b*) The effect of the axial non-uniformity on the critical inverse Strouhal number St_c^{-1}. Results are shown for the set-up described in §6 with pressure–flux boundary conditions, $\omega = 2\pi/T$, $\Sigma_0 = 0.6$ and $\Delta = 0.025$. Numerical simulations were performed with three values of α^2 at various values of Σ_1. The crosses are from simulations with $\ell = 10$, $z_1 = L/10$ and $z_2 = 9L/10$, while the circles are from simulations with $\ell = 17$, $z_1 = L/17$, and $z_2 = 9L/17$. From (6.1), we see that both these set-ups have the same theoretical predictions for St_c^{-1}. These predictions are shown as solid lines for the three values of α^2 considered.

Substituting $\Sigma_0 = 0.6$ into (D 4*b*), we obtain

$$\frac{1}{St_c} = \frac{3.80}{\alpha} \left[\frac{z_1}{a} + \frac{z_2 - z_1}{a} \int_0^1 \frac{1}{\Theta_2(0.6, \Sigma_1; \upsilon)^2} \frac{\Theta_1(0.6, \Sigma_1; \upsilon)^2}{\Theta_1(0.6, \Sigma_1; 0)^2} \, \mathrm{d}\upsilon \right], \qquad (6.1)$$

where the dimensionless functions Θ_i are defined in (D 5). A simpler form is not possible, since Θ_1 and hence the integral in (6.1) can only be evaluated numerically for individual values of Σ_1.

Figure 11(*b*) compares the asymptotic prediction (6.1) for St_c^{-1} (solid lines) against the numerical results (crosses) for a tube of aspect ratio $\ell = 10$ in which the upstream and downstream rigid sections each occupy 10 % of the tube length, i.e. $z_1 = L/10 = a$, $z_2 = 9L/10 = 9a$ as in §4. We performed computations for three values of the Womersley number α and a range of axial non-uniformities (parameterized by Σ_1). The agreement between the numerical and asymptotic results is very good and improves with increasing α.

The numerical and asymptotic results both predict an increase in St_c^{-1} with an increase in the axial non-uniformity Σ_1. Physically, this occurs because the smaller cross-sectional areas in the non-uniform section of the tube lead to increased axial velocities, and hence increased dissipation, for a given axial flux. With higher dissipative losses, more energy must be extracted from the background flow at the critical point. This can be achieved by having a larger background flow, which is equivalent to a larger $St^{-1} \propto \mathscr{U}$.

Over the range of axial non-uniformities considered here, the discrepancy between the numerical and asymptotic results increases slightly with increasing Σ_1, presumably because the increase in axial wall slope begins to violate the long-wavelength approximation employed in the asymptotic analysis. For even larger axial non-uniformities the flow is likely to separate in the downstream part of the oscillating section, invalidating the assumption that the flow remains attached to the walls throughout the oscillation.

The circular markers in figure 11(b) show the numerical results for St_c^{-1} for $\alpha^2 = 100$ with the same boundary conditions, tube shape and oscillation profile as before but with a longer downstream rigid section. The total length of the tube becomes $L = 17a$, but we keep $z_1 = a$ and $z_2 = 9a$. (This means that $\ell = 17$ and the lengths of the upstream, central and downstream sections are then in the ratio $1 : 8 : 8$ as in §5.) The agreement in figure 11(b) confirms the asymptotic prediction that for pressure–flux boundary conditions, St_c is independent of the length of the downstream rigid section, when the lengths of the upstream and central sections (given by z_1 and $z_2 - z_1$ respectively) are held fixed (see (6.1)). Furthermore, the agreement between the numerical results for the two cases shows that the imposition of a Poiseuille velocity profile in the outflow cross-section has little effect on the energetics of the flow even if the downstream rigid tube is relatively short, as it was for the $\ell = 10$ case.

7. Summary and conclusions

The main purpose of this paper was to show how the results of the theory developed in Part 1 of this work (Whittaker *et al.* 2010) could be applied to specific problems and to validate the theory by comparison with numerical simulations. A detailed discussion of the theory can be found in Part 1; so here we just summarize the results and findings from the present paper.

In §§4–6, we have shown excellent agreement between the asymptotic theory and numerical simulations performed using the `oomph-lib` library (Heil & Hazel 2006). Comparisons were performed for an elliptical tube undergoing a class of prescribed wall oscillations as described in §3. Both canonical sets of boundary conditions (pressure–flux and pressure–pressure) at the tube ends were considered, with simulations conducted with a range of parameter values for each.

For pressure–flux boundary conditions (§4), we obtained excellent agreement between the asymptotic predictions and the numerical results for the pressure and flow fields (figures 4 and 5) and the overall energetics of the system (figure 6). For pressure–pressure boundary conditions (§5), the agreement is not quite as good as that in the pressure–flux cases, but it is still very satisfying given the parameter values used: the ratios that should formally be 'small' in the asymptotic regime (2.7) were only around 0.1.

The numerical simulations with pressure–pressure boundary conditions revealed a slow adjustment phenomenon in the time-averaged axial flow. Reynolds stresses from the oscillatory flows cause an additional steady axial pumping effect (also seen in Jensen & Heil 2003), and the mean flow has to adjust from its value in the absence of oscillations. The magnitude of the pumping effect is well captured by the theory of Part 1, and in §5.2 we showed how the slow adjustment over many periods can be understood using a multiple-scale analysis. The change in the steady flux can have either sign, as shown by (2.14) and (2.16), but in the case in which kinetic energy is extracted from the mean flow ($|\tilde{V}(0)| > |\tilde{V}(1)|$), the steady flux will be increased. Although the slow adjustment to the mean flow is a relatively weak effect in the example presented here (figure 8), the pumping driven by unsteady Reynolds stresses is likely to have wider significance in the broader context of collapsible-tube flows. First, the capacity of a small oscillation to increase the mean flow through the tube, thereby increasing the potential source of energy to drive further oscillations, has been shown to be responsible for causing oscillations to arise subcritically (through essentially the same mechanism of energy transfer as described herein) in a one-dimensional model of a collapsible-channel flow (Stewart *et al.* 2009). The presence

of an additional slow time scale in the problem (figure 8) raises interesting questions about the nature of the bifurcation to instability in the full collapsible-tube problem. Second, adjustments to the mean flow (or mean pressure gradient) also have the capacity to increase the energy derived by work done by pressure forces at the channel inlet and therefore may play a key role in other mechanisms for self-excited oscillations. However, it should be noted that these theoretical predictions apply only in the specific regime considered here. Further calculations would be required to quantify the effects of changes to the steady flux in other regimes.

We also considered axially non-uniform tubes (§6) and again obtained good agreement between the asymptotic theory and numerical simulations. The chosen axial non-uniformity was found to increase the viscous dissipation. This reduces the rate at which energy is transferred to the wall and so increases the critical inverse Strouhal number St_c^{-1}. Figure 11(*b*) shows that even for moderate degrees of non-uniformity, St_c^{-1} does not change much from its value for a uniform tube ($\Sigma_1 = 0$).

The asymptotic theory of Part 1 is a critical step towards enabling the development of a fully rational theory for this class of instability in collapsible-tube flows. Having validated the theory against numerical simulations, we are currently extending the analysis to the case with full fluid–structure interaction. Normal modes of oscillation will be calculated, and the theory developed in Part 1 can then be used to determine the stability criterion for each mode. Results will be reported in future papers.

Appendix A. Coordinate system and geometry

For the calculations within the core region, we employ dimensionless elliptic cylindrical coordinates $(\sigma, \tau, \check{z})$, related to the previous dimensional Cartesian coordinates by

$$\frac{x}{a} = c \cosh \sigma \cos \tau, \qquad \frac{y}{a} = c \sinh \sigma \sin \tau, \qquad \frac{z}{L} = \check{z}, \qquad (A\,1a\text{--}c\,)$$

where c was defined in terms of $\sigma_0(z)$ in (3.2). Following (3.1) the tube occupies

$$\{(\sigma, \tau, \check{z}) \; : \; \sigma \in [0, \sigma_0(\check{z})], \; \tau \in [0, 2\pi), \; \check{z} \in [0, 1]\} \qquad (A\,2)$$

in the steady configuration. The elliptic coordinate system (A 1) has a single scale factor h, where

$$h(\sigma, \tau) = c(\sinh^2 \sigma + \sin^2 \tau)^{1/2} = c \left(\frac{\cosh 2\sigma - \cos 2\tau}{2} \right)^{1/2}, \qquad (A\,3)$$

which applies to both the σ and τ coordinates.

Unit vectors in the σ and τ directions respectively are given by

$$\hat{\boldsymbol{\sigma}} = \frac{c}{h}(\sinh \sigma \cos \tau \, \hat{\boldsymbol{x}} + \cosh \sigma \sin \tau \, \hat{\boldsymbol{y}}), \qquad (A\,4a)$$

$$\hat{\boldsymbol{\tau}} = \frac{c}{h}(-\cosh \sigma \sin \tau \, \hat{\boldsymbol{x}} + \sinh \sigma \cos \tau \, \hat{\boldsymbol{y}}). \qquad (A\,4b)$$

The triad of unit vectors aligned with the tube wall $\mathscr{W}_0$ in the steady configuration are related to $(\hat{\boldsymbol{\sigma}}, \hat{\boldsymbol{\tau}})$, by

$$\hat{\boldsymbol{n}} = \hat{\boldsymbol{\tau}} \cos\theta + \hat{\boldsymbol{z}} \sin\theta, \qquad \hat{\boldsymbol{t}} = \hat{\boldsymbol{\sigma}}, \qquad \hat{\boldsymbol{b}} = \hat{\boldsymbol{z}} \cos\theta - \hat{\boldsymbol{\tau}} \sin\theta, \qquad (\text{A}\,5a\text{–}c)$$

where θ is the angle of the wall to the tube axis. (The angle θ is related to the factor G defined in Part 1 by $G = \ell \sin\theta$.) For the elliptical cross-sections considered here, θ can be determined by

$$\tan\theta = \frac{\hat{\boldsymbol{t}} \cdot \dfrac{\partial \boldsymbol{r}_0}{\partial \check{Z}}\bigg|_{\check{Y}}}{\hat{\boldsymbol{z}} \cdot \dfrac{\partial \boldsymbol{r}_0}{\partial \check{Z}}\bigg|_{\check{Y}}} = \frac{ac}{2h\ell} \frac{\mathrm{d}c}{\mathrm{d}\check{z}} \sinh 2\sigma_0 + \frac{ac^2}{h\ell} \frac{\mathrm{d}\sigma_0}{\mathrm{d}\check{z}} (\cosh^2 \sigma_0 - \cos^2 \check{Y}). \qquad (\text{A}\,6)$$

Since the axial variation is slow, $\theta \ll 1$, and near the tube wall, the boundary-layer coordinates $(\check{X}, \check{Y}, \check{Z})$ introduced in Part 1 are almost aligned with the elliptical coordinates used in the cross-section. The surface scale factor $H_{\check{Y}}^{\mathrm{s}}$ is related to h by $H_{\check{Y}}^{\mathrm{s}}(\check{Y}, \check{Z}) = h(\sigma_0, \check{Y})$. At leading order, we have

$$\check{X} = \frac{h(\sigma_0, \tau)}{\epsilon}(\sigma_0 - \sigma), \qquad \check{Y} = \tau, \qquad \check{Z} = \check{z}. \qquad (\text{A}\,7a\text{–}c)$$

In the steady configuration, the tube has cross-sectional area

$$A_0 = a^2 \int_0^{2\pi} \int_0^{\sigma_0} h^2 \, \mathrm{d}\sigma \, \mathrm{d}\tau = \frac{1}{2}\pi a^2 c^2 \sinh 2\sigma_0, \qquad (\text{A}\,8)$$

and the length of the perimeter of each cross-section is given by

$$C_0 = a \int_0^{2\pi} h(\sigma_0, \tau) \, \mathrm{d}\tau = \frac{4ac\,\mathrm{Ee}(\operatorname{sech}\sigma_0)}{\operatorname{sech}\sigma_0}, \qquad (\text{A}\,9)$$

where Ee is the complete elliptic integral of the second kind, as defined in (3.3).

Using expression (A 8) for A_0, the angle θ may be re-expressed as

$$\tan\theta = \frac{1}{2\pi a h\ell} \frac{\mathrm{d}A_0}{\mathrm{d}\check{z}} - \frac{ac^2}{2h\ell} \frac{\mathrm{d}\sigma_0}{\mathrm{d}\check{z}} \cos(2\check{Y}). \qquad (\text{A}\,10)$$

Given the deformations (3.6), the dimensionless area change within each cross-section is

$$\tilde{A}(\check{z}) = \int_0^{2\pi} \xi(\check{Y}, \check{z}) \, H_{\check{Y}}^{\mathrm{s}} H_{\check{Z}}^{\mathrm{s}} \, \mathrm{d}\check{Y} = -\frac{3\pi d(\check{z})}{2\cosh 2\sigma_0}. \qquad (\text{A}\,11)$$

Appendix B. Solution for an elliptical tube with pressure–flux boundary conditions

In this Appendix we apply the methods developed in Part 1 (Whittaker *et al.* 2010) to solve the problem studied in §4 of the present paper, namely that of flow through an initially uniform elliptical tube with oscillating walls of the form described in §3. As well as computing the energy transfer E from the fluid to the tube walls (2.13a) and the critical Strouhal number at which this vanishes (2.13b), we calculate the asymptotic solution for the pressure and velocity fields. The notation used throughout this Appendix is that defined in Part 1.

B.1. *Energy transfer and critical inverse Strouhal number*

We note that $\tilde{A}$ is given by (A 11) and that $\chi = \Psi = 0$, since we have pressure–flux boundary conditions. Then, from (2.10) we find that

$$\tilde{\mathbb{V}}(\check{z}) = \frac{3\pi(\check{z}_2 - \check{z}_1)}{4\cosh 2\sigma_0} \begin{cases} 1 & : \quad 0 < \check{z} < \check{z}_1, \\ \dfrac{\check{z}_2 - \check{z}}{\check{z}_2 - \check{z}_1} + \dfrac{1}{2\pi}\sin\left(\dfrac{2\pi(\check{z} - \check{z}_1)}{\check{z}_2 - \check{z}_1}\right) & : \quad \check{z}_1 < \check{z} < \check{z}_2, \\ 0 & : \quad \check{z}_2 < \check{z} < 1, \end{cases} \tag{B 1}$$

where $\check{z} = z/L$ is the dimensionless axial coordinate and $\check{z}_i = z_i/L$ are the dimensionless positions of the joints between the rigid and flexible sections of the tube.

The mean energy transfer to the wall and critical inverse Strouhal number are then found from (2.13) to be

$$\frac{E}{\mathbb{E}} = \frac{9\pi\check{\omega}^2(\check{z}_2 - \check{z}_1)^2}{32\cosh^2 2\sigma_0}\left(\frac{1}{St} - \frac{1}{St_c}\right), \tag{B 2}$$

$$\frac{1}{St_c} = \frac{4\ell}{\alpha}\left(\frac{\check{\omega}}{\sinh 2\sigma_0}\right)^{1/2}\frac{\mathrm{Ee}(\mathrm{sech}\,\sigma_0)}{\pi\,\mathrm{sech}\,\sigma_0}\left[\frac{1}{2}(\check{z}_1 + \check{z}_2) - \left(\frac{1}{6} - \frac{5}{8\pi^2}\right)(\check{z}_2 - \check{z}_1)\right], \tag{B 3}$$

where $\check{\omega} = \omega T$ is the dimensionless frequency.

B.2. *The leading-order steady flow*

Since the tube is uniform in z in the steady configuration, we assume that the leading-order steady flow is a uniform fully developed Poiseuille flow. From Part 1 (4.3)–(4.5) this must satisfy

$$\left(\frac{\partial^2}{\partial\sigma^2} + \frac{\partial^2}{\partial\tau^2}\right)\bar{w}_0 = -\mathscr{G}[h(\sigma,\tau)]^2 \quad \text{in } \sigma < \sigma_0, \tag{B 4}$$

where $\mathscr{G} = -(R^2/\epsilon\lambda)(\mathrm{d}\bar{p}'/\mathrm{d}\check{z})$ is the uniform scaled pressure gradient, subject to

$$\bar{w}_0(\sigma_0, \tau) = 0, \tag{B 5a}$$

$$\bar{w}_0(0, \tau) = \bar{w}_0(0, 2\pi - \tau), \tag{B 5b}$$

$$\frac{\partial\bar{w}_0}{\partial\sigma}(0, \tau) = -\frac{\partial\bar{w}_0}{\partial\sigma}(0, 2\pi - \tau), \tag{B 5c}$$

$$\int_0^{2\pi}\int_0^{\sigma_0}\bar{w}_0\,h^2\,\mathrm{d}\sigma\,\mathrm{d}\tau = \pi. \tag{B 5d}$$

We obtain the solution

$$\bar{w}_0 = 2\coth^2 2\sigma_0\left(1 - \frac{\cosh 2\sigma}{\cosh 2\sigma_0}\right)\left(1 - \frac{\cos 2\tau}{\cosh 2\sigma_0}\right), \tag{B 6}$$

with $\mathscr{G} = 8\coth 2\sigma_0$. Equation (B 6) can also be expressed more simply in terms of the Cartesian coordinates as

$$\bar{w}_0 = 2\left[1 - \left(\frac{\check{x}}{c\cosh\sigma_0}\right)^2 - \left(\frac{\check{y}}{c\sinh\sigma_0}\right)^2\right]. \tag{B 7}$$

Since we have a flux boundary condition at one end of the tube, we have $\bar{w}_\spadesuit = \bar{w}_0$.

Following §7 of Part I, the leading-order axial pressure in the core is given by $\bar{p}_\phi = \Pi + \bar{p}'$, where

$$\bar{p}' = -\frac{8\epsilon\lambda\coth 2\sigma_0}{R^2}z, \tag{B 8a}$$

$$\Pi = -\frac{1}{4}(\lambda\delta)^2(|\tilde{w}_{00}(\check{z})|^2 - |\tilde{w}_{00}(0)|^2), \tag{B 8b}$$

and the expression for $\tilde{w}_{00}(\check{z})$ is given in (B 9).

B.3. *The leading-order oscillatory flow in the core*

Part 1 equations (5.13a) and (5.13b) give the expressions for the leading-order axial velocity and pressure in the core in terms of $\tilde{V}(\check{z})$. Using (B 1), we find that

$$\tilde{w}_{00} = -\frac{3i\check{\omega}(\check{z}_2 - \check{z}_1)}{4\cosh 2\sigma_0}\begin{cases} 1 & : \quad 0 < \check{z} < \check{z}_1, \\ \dfrac{\check{z}_2 - \check{z}}{\check{z}_2 - \check{z}_1} + \dfrac{1}{2\pi}\sin\left(\dfrac{2\pi(\check{z} - \check{z}_1)}{\check{z}_2 - \check{z}_1}\right) & : \quad \check{z}_1 < \check{z} < \check{z}_2, \\ 0 & : \quad \check{z}_2 < \check{z} < 1 \end{cases} \tag{B 9}$$

and

$$\tilde{p}_{00} = -\frac{3\check{\omega}^2}{8\cosh 2\sigma_0}$$
$$\times\begin{cases} 2z(\check{z}_2 - \check{z}_1) & : \quad 0 < \check{z} < \check{z}_1, \\ -(\check{z} - \check{z}_2)^2 + (\check{z}_2^2 - \check{z}_1^2) + \left(\dfrac{\check{z}_2 - \check{z}_1}{\pi}\right)^2\sin^2\left(\dfrac{\pi(\check{z} - \check{z}_1)}{\check{z}_2 - \check{z}_1}\right) & : \quad \check{z}_1 < \check{z} < \check{z}_2, \\ \check{z}_2^2 - \check{z}_1^2 & : \quad \check{z}_2 < \check{z} < 1. \end{cases} \tag{B 10}$$

From Part 1 (5.19)–(5.22) and Part 2 (2.9), the Poisson problem for $\tilde{p}_{01}^\triangle$ is

$$\check{\nabla}_\perp^2\tilde{p}_{01}^\triangle = \frac{\check{\omega}^2\beta\,\tilde{A}(\check{z})}{\pi} = -\frac{3\check{\omega}^2\beta\,d(\check{z})}{4\cosh 2\sigma_0}, \tag{B 11}$$

and hence

$$\left(\frac{\partial^2}{\partial\sigma^2} + \frac{\partial^2}{\partial\tau^2}\right)\tilde{p}_{01}^\triangle = -\frac{3\check{\omega}^2\beta\,d(\check{z})}{\sinh 4\sigma_0}\left(\cosh 2\sigma - \cos 2\tau\right), \tag{B 12}$$

subject to

$$\frac{\partial\tilde{p}_{01}^\triangle}{\partial\sigma}(\sigma_0, \tau) = \check{\omega}^2\beta\,d(\check{z})\left(-\frac{3\,\text{sech}\,2\sigma_0}{4} + \cos 2\tau - \frac{\text{sech}\,2\sigma_0}{4}\cos 4\tau\right), \tag{B 13}$$

$$\tilde{p}_{01}^\triangle(0, \tau) = \tilde{p}_{01}^\triangle(0, 2\pi - \tau), \qquad \frac{\partial\tilde{p}_{01}^\triangle}{\partial\sigma}(0, \tau) = -\frac{\partial\tilde{p}_{01}^\triangle}{\partial\sigma}(0, 2\pi - \tau), \tag{B 14a,b}$$

$$\int_0^{2\pi}\int_0^{\sigma_0}\tilde{p}_{01}^\triangle h^2\,d\sigma\,d\tau = 0. \tag{B 15}$$

The solution to (B 12)–(B 15) is

$$\tilde{p}_{01}^{\triangle}(\sigma, \tau, z) = -\frac{3\breve{\omega}^2 \beta d(\breve{z})}{4 \sinh 4\sigma_0} \left(\cosh 2\sigma + \cos 2\tau - \frac{1}{2} \cosh 2\sigma_0 \right)$$

$$+ \frac{\breve{\omega}^2 \beta d(\breve{z})}{2 \sinh 2\sigma_0} \left(\cosh 2\sigma \cos 2\tau + \frac{1}{2} \right)$$

$$- \frac{\breve{\omega}^2 \beta d(\breve{z})}{16 \cosh 2\sigma_0 \sinh 4\sigma_0} \cosh 4\sigma \cos 4\tau. \tag{B 16}$$

The three parts correspond precisely to the three terms in the normal boundary displacement ξ and hence in the boundary condition (B 13). The first part is a particular integral for (B 12), and the other two parts satisfy the homogeneous equation. All three parts individually satisfy the remaining three constraints (B 14)–(B 15).

The flow in the cross-section can then be recovered from Part 1 (5.7b), which gives

$$\hat{\boldsymbol{\sigma}} \cdot \tilde{\boldsymbol{u}}_{00} = \frac{i\breve{\omega} d(\breve{z})}{h(\sigma, \tau)} \left(-\frac{3 \sinh 2\sigma}{2 \sinh 4\sigma_0} + \frac{\sinh 2\sigma \cos 2\tau}{\sinh 2\sigma_0} - \frac{\sinh 4\sigma \cos 4\tau}{4 \cosh 2\sigma_0 \sinh 4\sigma_0} \right), \tag{B 17a}$$

$$\hat{\boldsymbol{\tau}} \cdot \tilde{\boldsymbol{u}}_{00} = \frac{i\breve{\omega} d(\breve{z})}{h(\sigma, \tau)} \left(\frac{3 \sin 2\tau}{2 \sinh 4\sigma_0} - \frac{\cosh 2\sigma \sin 2\tau}{\sinh 2\sigma_0} + \frac{\cosh 4\sigma \sin 4\tau}{4 \cosh 2\sigma_0 \sinh 4\sigma_0} \right). \tag{B 17b}$$

B.4. *The leading-order oscillatory flow in the Stokes layer*

Expressions for the boundary-layer velocities are given in Part 1 (5.6a) and Part 1 (5.27), in terms of the wall displacements (ξ, η, ζ), the outer limit of the core flow $\tilde{\boldsymbol{u}}_{00}(\sigma_0, Y, Z)$ and the scaled normal coordinate X. These can be re-expressed in terms of the elliptic coordinates in the core, using (A 7). We obtain

$$\tilde{U}_{00} = i\breve{\omega} \xi(\tau, \breve{z}) = \hat{\boldsymbol{\sigma}}(\sigma_0, \tau) \cdot \tilde{\boldsymbol{u}}_{00}(\sigma_0, \tau, \breve{z}), \tag{B 18a}$$

$$\tilde{V}_{00} = \hat{\boldsymbol{\tau}}(\sigma_0, \tau) \cdot \tilde{\boldsymbol{u}}_{00}(\sigma_0, \tau, \breve{z}) [1 - E(\sigma, \tau)] + i\breve{\omega} \eta(\tau, \breve{z}) E(\sigma, \tau), \tag{B 18b}$$

$$\tilde{W}_{00} = \tilde{w}_{00}(\sigma_0, \tau, \breve{z}) [1 - E(\sigma, \tau)], \tag{B 18c}$$

where, from Part 1 (5.28), the boundary-layer decay function is given by

$$E(\sigma, \tau) = \exp \left[-\left(\frac{\breve{\omega}}{2} \right)^{1/2} \frac{(1 + i)R}{\epsilon} h(\sigma_0, \tau) (\sigma_0 - \sigma) \right]. \tag{B 19}$$

B.5. *The first-order corrections to the oscillatory flow in the core*

The first-order correction to the pressure in the core is given by $\tilde{p}_{01} = \tilde{p}_{01}^* + \tilde{p}_{01}^{\triangle}$. The second term has already been calculated above; the first term is found by integrating Part 1 (5.37) and applying the boundary conditions $\tilde{p}_{01}^*(0) = 0$ and $\mathrm{d}\tilde{p}_{01}^*/\mathrm{d}\breve{z}(1) = 0$. We obtain

$$\tilde{p}_{01}^*(\breve{z}) = \frac{(1 - i)C_0}{\pi (2\breve{\omega})^{1/2} R} \tilde{p}_{00}(z) - \frac{2}{\lambda} (\tilde{w}_{00}(\breve{z}) - \tilde{w}_{00}(0)). \tag{B 20}$$

The pressure is closely linked to the axial velocity. At leading order, this was seen to be plug flow with a flux set by continuity. The first term in (B 20) adjusts the plug-flow flux by $O(\epsilon)$ to correct for the reduction of the axial velocity in the Stokes layer. The second term in (B 20) represents the additional pressure gradient required to balance the Reynolds stresses in the core. The additional flow it induces has zero cross-sectional average at this order.

The associated axial velocity is then recovered from (B 20) using Part 1 (5.31c). We obtain

$$\tilde{w}_{01} = \frac{(1-\mathrm{i})C_0}{\pi(2\check{\omega})^{1/2}R}\tilde{w}_{00} + \frac{\mathrm{i}}{\check{\omega}\lambda}\left(\tilde{\boldsymbol{u}}_{00}^{\perp}\cdot\check{\nabla}_{\perp}\overline{w}_{\phi} + (\overline{w}_{\phi}-2)\frac{\mathrm{d}\tilde{w}_{00}}{\mathrm{d}\check{z}}\right) + \frac{\mathrm{i}}{\check{\omega}}\frac{\partial\tilde{p}_{01}^{\triangle}}{\partial\check{z}}. \qquad \text{(B 21)}$$

The first term represents the change in the magnitude of the plug-flow component to account for the reduced flux in the Stokes layer. The second group of terms is the response to the Reynolds stresses. The final term is the response to axial variations in deviations from the mean pressure in each cross-section.

Similar corrections can also be calculated for the cross-sectional transverse velocity $\tilde{\boldsymbol{u}}_{01}^{\perp}$ in the core and the $O(\epsilon)$ velocity in the Stokes boundary layers. However, satisfactory agreement with the numerical calculations has been obtained without the need for these corrections.

B.6. *Composite expansions*

We have now computed the oscillatory axial velocity and pressure in the core to $O(\epsilon)$, and the oscillatory transverse velocity in the core and all the boundary-layer variables to $O(1)$.

The $O(\epsilon)$ oscillatory pressure is uniform across the boundary layer; so we are able to form a composite expansion accurate to $O(\epsilon)$ in the oscillatory component. We have

$$\frac{Tp_{comp}}{\rho L\mathscr{U}} = \check{p}_{comp} = \frac{\epsilon}{\lambda}(\vec{p}_0' + \overline{\Pi}) + \lambda\delta\,\mathrm{Re}\{\mathrm{e}^{\mathrm{i}\check{\omega}\check{t}}[\tilde{p}_{00} + \epsilon(\tilde{p}_{01}^* + \tilde{p}_{01}^{\triangle})]\} + \cdots, \qquad \text{(B 22)}$$

where the steady components are given by (B 8b) and (B 8a) and the oscillatory components by (B 10), (B 16) and (B 20).

For the velocities, we have not computed the $O(\epsilon)$ oscillatory behaviour in the Stokes layer; so the composite expansions can only be given to leading order in the oscillatory flow. The axial velocity $\tilde{w}$ is uniform in the core at leading order; so the composite expansion is simply the boundary-layer expression Part 1 (5.27b). We have

$$\frac{w_{comp}}{\mathscr{U}} = \check{w}_{comp} = \overline{w}_{\phi} + \lambda\delta\,\mathrm{Re}\{\mathrm{e}^{\mathrm{i}\check{\omega}\check{t}}\,\tilde{w}_{00}[1-E(\sigma,\tau)]\} + \cdots, \qquad \text{(B 23)}$$

where $E(\sigma,\tau)$ is given (B 19), $\overline{w}_{\phi} = \overline{w}_0$ by (B 6) and $\tilde{w}_{00}$ by (B 9).

The transverse oscillatory velocity component $\hat{\boldsymbol{\sigma}}\cdot\tilde{\boldsymbol{u}}^{\perp}$ is uniform across the boundary layer at leading order; so the composite expansion is formed using just the expression that applies in the core. There is no steady component to the transverse velocity; so we have

$$\frac{\ell}{\mathscr{U}}\hat{\boldsymbol{\sigma}}\cdot\boldsymbol{u}_{comp}^{\perp} = \hat{\boldsymbol{\sigma}}\cdot\check{\boldsymbol{u}}_{comp}^{\perp} = \lambda\delta\,\mathrm{Re}\{\mathrm{e}^{\mathrm{i}\check{\omega}\check{t}}\,\hat{\boldsymbol{\sigma}}\cdot\tilde{\boldsymbol{u}}_{00}^{\perp}\} + \cdots, \qquad \text{(B 24)}$$

where $\hat{\boldsymbol{\sigma}}\cdot\tilde{\boldsymbol{u}}_{00}^{\perp}$ is given by (B 17a).

For the transverse oscillatory velocity component $\hat{\boldsymbol{\tau}}\cdot\tilde{\boldsymbol{u}}^{\perp}$, we must sum the core and boundary-layer expressions and then subtract off the common limiting value. Again there is no steady component. We obtain

$$\frac{\ell}{\mathscr{U}}\hat{\boldsymbol{\tau}}\cdot\boldsymbol{u}_{comp}^{\perp} = \hat{\boldsymbol{\tau}}\cdot\check{\boldsymbol{u}}_{comp}^{\perp} = \lambda\delta\,\mathrm{Re}\{\mathrm{e}^{\mathrm{i}\check{\omega}\check{t}}[\hat{\boldsymbol{\tau}}\cdot\tilde{\boldsymbol{u}}_{00}^{\perp}(1-E(\sigma,\tau)) + \mathrm{i}\check{\omega}\,\eta(\tau,z)\,E(\sigma,\tau)]\} + \cdots,$$
$$\text{(B 25)}$$

where $E(\sigma,\tau)$ is as defined in (B 19) and $\hat{\boldsymbol{\tau}}\cdot\tilde{\boldsymbol{u}}_{00}^{\perp}$ is given by (B 17b).

Finally, we note that the expression for the axial velocity in the core, correct to $O(\epsilon)$ in the oscillatory component, is given by

$$\frac{w}{\mathscr{U}} = \breve{w} = \bar{u}_\phi + \lambda\delta\,\mathrm{Re}\{e^{i\breve{\omega}\breve{t}}(\tilde{w}_{00} + \epsilon\tilde{w}_{01})\} + \cdots, \tag{B 26}$$

where the steady component is given by (B 6) and the unsteady components by (B 9) and (B 21).

Appendix C. Solution for an elliptical tube with pressure–pressure boundary conditions

Here we consider the problem studied in §5, namely that of flow through an initially uniform elliptical tube with oscillating walls of the form described in §3. As well as computing the energy transfer E from the fluid to the tube walls (2.13a), and the critical Strouhal number at which this vanishes (2.13b), we explicitly calculate the change in the flux due to the presence of the oscillations. For brevity, we do not present the calculations for the velocity and pressure fields.

The tube is uniform with $A_0 = \pi a^2$ and $\tilde{A}(z)$ given by (A 11). From (2.11) we have $\chi = z/L \equiv \breve{z}$, and then using (2.10) we obtain

$$\tilde{\mathbb{V}}(\breve{z}) = \frac{3\pi(\breve{z}_2 - \breve{z}_1)}{4\cosh 2\sigma_0}\,f(\breve{z}), \tag{C 1}$$

where

$$f(\breve{z}) = \begin{cases} 1 - \dfrac{\breve{z}_2 + \breve{z}_1}{2} & : \quad 0 < \breve{z} < \breve{z}_1, \\[2mm] -\dfrac{\breve{z}_2 + \breve{z}_1}{2} + \dfrac{\breve{z}_2 - z}{\breve{z}_2 - \breve{z}_1} + \dfrac{\breve{z}_2 - \breve{z}_1}{2\pi}\sin\left(\dfrac{2\pi(z - \breve{z}_1)}{\breve{z}_2 - \breve{z}_1}\right) & : \quad \breve{z}_1 < \breve{z} < \breve{z}_2, \\[2mm] -\dfrac{\breve{z}_2 + \breve{z}_1}{2} & : \quad \breve{z}_2 < \breve{z} < 1, \end{cases} \tag{C 2}$$

and $\breve{z}_i = z_i/L$ as before.

We now calculate the flux correction factor Ψ from (2.14) and the energy flux and critical Strouhal number using (2.13). From the definition in (2.15) and the calculations in §B.2, we find that $k^{-1} = 8\coth 2\sigma_0$. We then obtain

$$\Psi = \frac{9\alpha^2\ell\Delta^2\breve{\omega}^2(\breve{z}_2 - \breve{z}_1)^2}{512\coth 2\sigma_0\cosh^2 2\sigma_0}[1 - (\breve{z}_1 + \breve{z}_2)], \tag{C 3}$$

$$\frac{E}{\mathbb{E}} = \frac{9\pi\breve{\omega}^2(\breve{z}_2 - \breve{z}_1)^2}{32\cosh^2 2\sigma_0}(1 - (\breve{z}_1 + \breve{z}_2))\left(\frac{1}{St} - \frac{1}{St_c}\right), \tag{C 4}$$

$$\begin{aligned} \frac{1}{St_c} &= \frac{4\ell}{\alpha}\left(\frac{\breve{\omega}}{\sinh 2\sigma_0}\right)^{1/2}\frac{\mathrm{Ee}(\mathrm{sech}\,\sigma_0)}{\mathrm{sech}\,\sigma_0}\frac{1}{1 - (\breve{z}_1 + \breve{z}_2)} \\[2mm] &\quad \times\left\{\frac{1}{2}(\breve{z}_1 + \breve{z}_2)\left[1 - \tfrac{1}{2}(\breve{z}_1 + \breve{z}_2)\right] - \left(\frac{1}{6} - \frac{5}{8\pi^2}\right)(\breve{z}_2 - \breve{z}_1)\right\} \\[2mm] &\quad - \frac{9\alpha^2\ell\Delta^2\breve{\omega}^2(\breve{z}_2 - \breve{z}_1)^2}{512\coth 2\sigma_0\cosh^2 2\sigma_0}[1 - (\breve{z}_1 + \breve{z}_2)], \end{aligned} \tag{C 5}$$

where $\breve{\omega} = \omega T$ is the dimensionless frequency.

Finally, we can compute the steady flux from (2.16) as

$$Q = \pi a^2\mathscr{U}\left\{1 + \frac{9\alpha^2\ell St\,\Delta^2\breve{\omega}^2(\breve{z}_2 - \breve{z}_1)^2}{512\coth 2\sigma_0\cosh^2 2\sigma_0}[1 - (\breve{z}_1 + \breve{z}_2)]\right\}. \tag{C 6}$$

Observe that in the limit $\ell \to \infty$, $\check{z}_1, \check{z}_2 \to 0$ with $\ell\check{z}_1$ and $\ell\check{z}_2$ held fixed, the pair of expressions (C 4) and (C 5) become identical with the corresponding expressions (B 2) and (B 3) for the pressure–flux case. Physically, this limit corresponds to lengthening the downstream rigid section of the tube while keeping the other dimensions fixed. In this limit the two different downstream boundary conditions become equivalent, as both have the effect of suppressing the oscillatory axial flow at the downstream end. In the case of the flux condition, this suppression is achieved directly by the flux condition itself. With the pressure condition, it is the large inertance (resistance to oscillatory flow) of the fluid in the long downstream section that suppresses the oscillations there.

Appendix D. Solution for axially non-uniform steady configuration

Here we consider the problem studied in §5, namely flow through an initially non-uniform elliptical tube with oscillating walls of the form described in §3. For brevity, we just present the calculations for the energy transfer E from the fluid to the tube walls, and the critical Strouhal number St_c^{-1} at which this vanishes, for the case of pressure–flux boundary conditions with oscillations of frequency $\omega = 2\pi/T$.

From (2.18) and (A 11) we have that the oscillatory volume flux is given by

$$\tilde{V}(\check{z}) = \frac{3\pi}{2} \int_{\check{z}}^{1} \frac{d(\check{z}')}{\cosh[2\sigma_0(\check{z}')]} \, d\check{z}', \qquad (D\,1)$$

where the axial variations of d and σ_0 are given by (3.7) and (3.5); $\tilde{V}(\check{z})$ can only be evaluated numerically.

From (A 8) and (3.2), the cross-sectional area in the steady configuration is given by

$$A_0(\check{z}) = \pi a^2 \frac{\tanh[\sigma_0(\check{z})]}{\tanh \Sigma_0} \left(\frac{\mathrm{Ee}[\mathrm{sech}\,\Sigma_0]}{\mathrm{Ee}[\mathrm{sech}\,\sigma_0(\check{z})]} \right)^2, \qquad (D\,2)$$

and using (A 9) and (2.8) the relative perimeter is found to be

$$\mathbb{P}(\check{z}) = \frac{2\mathrm{Ee}(\mathrm{sech}[\sigma_0(\check{z})])}{\pi(\tanh[\sigma_0(\check{z})])^{1/2}}. \qquad (D\,3)$$

Expressions (D 1)–(D 3) along with expressions (3.5) and (3.7) for $\sigma_0(\check{z})$ and $d(\check{z})$ are then substituted into (2.17), to obtain the required results for E and St_c. The integration required must again be completed numerically, and we obtain

$$\frac{E}{\mathbb{E}} = 2\pi(\check{z}_2 - \check{z}_1)^2 f(\Sigma_0, \Sigma_1; 0)^2 \left(\frac{1}{St} - \frac{1}{St_c} \right), \qquad (D\,4a)$$

$$\frac{1}{St_c} = \frac{\ell}{\alpha} \frac{4\,\mathrm{Ee}(\mathrm{sech}\,\Sigma_0)}{(\pi \tanh \Sigma_0)^{1/2}} \left[\check{z}_1 + (\check{z}_2 - \check{z}_1) \int_0^1 \frac{1}{\Theta_2(\Sigma_0, \Sigma_1; \upsilon)^2} \frac{\Theta_1(\Sigma_0, \Sigma_1; \upsilon)^2}{\Theta_1(\Sigma_0, \Sigma_1; 0)^2} \, d\upsilon \right], \qquad (D\,4b)$$

where

$$\Theta_1(\Sigma_0, \Sigma_1; \upsilon) = \frac{3\pi}{2} \int_{\upsilon}^{1} \frac{\sin^2 \pi\upsilon'}{\cosh 2(\Sigma_0 - \Sigma_1 \sin^2 \pi\upsilon')} \, d\upsilon', \qquad (D\,5a)$$

$$\Theta_2(\Sigma_0, \Sigma_1; \upsilon) = \frac{\tanh(\Sigma_0 - \Sigma_1 \sin^2 \pi\upsilon)}{\tanh \Sigma_0} \left(\frac{\mathrm{Ee}[\mathrm{sech}\,\Sigma_0]}{\mathrm{Ee}[\mathrm{sech}(\Sigma_0 - \Sigma_1 \sin^2 \pi\upsilon)]} \right)^2 \qquad (D\,5b)$$

and $\check{z}_i = z_i/L$ as before.

REFERENCES

BERTRAM, C. D. 2003 Experimental studies of collapsible tubes. In *Flow Past Highly Compliant Boundaries and in Collapsible Tubes* (ed. P. W. Carpenter & T. J. Pedley), chap. 3, pp. 51–65. Kluwer Academic.

BERTRAM, C. D. & TSCHERRY, J. 2006 The onset of flow-rate limitation and flow-induced oscillations in collapsible tubes. *J. Fluids Struct.* **22**, 1029–1045.

DAVIES, C. & CARPENTER, P. W. 1997 Instabilities in a plane channel flow between compliant walls. *J. Fluid Mech.* **352**, 205–243.

GROTBERG, J. B. & JENSEN, O. E. 2004 Biofluid mechanics in flexible tubes. *Annu. Rev. Fluid Mech.* **36**, 121–147.

HEIL, M. & HAZEL, A. L. 2006 `Oomph-lib` – an object-oriented multi-physics finite-element library. In *Fluid–Structure Interaction* (ed. H.-J. Bungartz & M. Schäfer), pp. 19–49. Springer. (`Oomph-lib` is available as open-source software at http://www.oomph-lib.org/.)

HEIL, M. & WATERS, S. L. 2006 Transverse flows in rapidly oscillating elastic cylindrical shells. *J. Fluid Mech.* **547**, 185–214.

HEIL, M. & WATERS, S. L. 2008 How rapidly oscillating collapsible tubes extract energy from a viscous mean flow. *J. Fluid Mech.* **601**, 199–227.

JENSEN, O. E. 1990 Instabilities of flow in a collapsed tube. *J. Fluid Mech.* **220**, 623–659.

JENSEN, O. E. & HEIL, M. 2003 High-frequency self-excited oscillations on a collapsible-channel flow. *J. Fluid Mech.* **481**, 235–268.

LUO, X. Y., CAI, Z., LI, W. G. & PEDLEY, T. J. 2008 The cascade structure of linear instability in collapsible channel flows. *J. Fluid Mech.* **600**, 45–76.

MORTENSEN, N. A. & BRUUS, H. 2006 Universal dynamics in the onset of a Hagen–Poiseuille flow. *Phys. Rev.* E **74**, 017301.

STEWART, P. S., WATERS, S. L. & JENSEN, O. E. 2009 Local and global instabilities of flow in a flexible-walled channel. *Eur. J. Mech.* B **28** (4), 541–557.

TROESCH, B. A. & TROESCH, H. R. 1973 Eigenfrequencies of an elliptic membrane. *Math. Comp.* **27** (124), 755–765.

WHITTAKER, R. J., WATERS, S. L., JENSEN, O. E., BOYLE, J. & HEIL, M. 2010 The energetics of flow through a rapidly oscillating tube. Part 1. General theory. *J. Fluid Mech.* **648**, 83–121.